Review

Carbon Future

Photo-thermo synergistic catalysis for methane conversion

Chengzhi Guo, Xiyi Li✉, and Yang Lan✉

Department of Chemical Engineering, University College London, Gower Street, London, WC1E 7JE, UK

Cite This: *Carbon Future* **2026**, *3*, 9200067

Read Online

ABSTRACT: The direct conversion of abundant methane into valuable products represents a promising strategy for constructing new chemical synthesis networks. However, conventional thermocatalysis often suffers from moderate selectivity and stability due to the harsh reaction conditions required for methane activation, while photocatalysis typically exhibits low conversion rates owing to intrinsic limitations such as charge recombination and poor mass transfer. Photo-thermo synergistic catalysis has emerged as a next-generation approach that integrates photo and thermal energy inputs, leveraging photons to overcome activation barriers and phonons to accelerate bulk/surface kinetics, thereby addressing the limitations of single-energy systems. In this review, we clarify the advantages and limitations of dual-energy versus single-energy approaches, explain four distinct synergistic modes between photo and thermo, and summarise recent strategies for methane valorisation into a range of valuable products. We also discuss the roles of photon and phonon in modulating reaction kinetics and product selectivity. Finally, we propose insights into current challenges and potential solutions, including scientific performance evaluation, expansion of product scope, development of dual-energy *in-situ* characterisation techniques, photo-thermo reactor design, and AI-driven catalyst discovery.

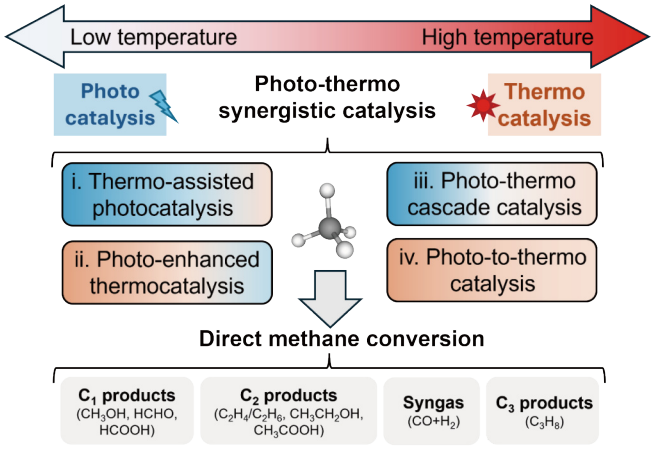

KEYWORDS: photo-thermo synergistic catalysis, methane conversion, C–H activation, selectivity.

1 Introduction

Methane, the primary component of natural gas, biogas, shale gas and combustible ice, is an abundant and readily accessible C_1 building block for constructing diverse chemical synthesis networks[1–4]. Beyond its industrial relevance, the direct conversion of methane also offers substantial environmental benefits, as methane is a potent greenhouse gas[5].

However, methane is an exceptionally inert molecule due to its symmetrical tetrahedral geometry, strong C–H bonding energy (439 kJ·mol^{-1}), negligible electron affinity, and low polarisability[4, 6]. Consequently, conventional thermocatalytic conversion requires harsh reaction conditions to overcome the significant kinetic barrier, typically involving high temperatures (600–1100 °C), elevated pressures (30–200 bars), and strong oxidants[7–9]. These conditions impose several limitations on direct methane conversion: 1) the reaction tends to favour thermodynamically stable byproducts such as coke, CO_2, driven by overheated and disordered reaction pathways[10, 11]; 2) the non-selective, three-dimensional energy input leads to excessive molecular vibrations and energy dissipation, reducing overall energy efficiency[10]. As a result, despite decades of research, the yield and selectivity of direct methane conversion remain insufficient to justify the high energy input, capital costs, limited catalyst lifetimes, and associated carbon footprint.

Photocatalysis, which utilises photons as an alternative driving force, offers a promising strategy to overcome the kinetic-thermodynamic constraints associated with methane activation[6, 12–15]. Specifically: 1) the targeted delivery of high-energy input (a few eV) to selected molecules enables the circumvention of thermodynamic equilibrium constraints; 2) photoexcited charge carriers can preactivate the C–H bond, thereby reducing the activation energy. Consequently, photocatalytic methane conversion has achieved notable success in producing a variety of value-added products, such as ethane/ethylene, benzene, methanol, ethanol and formaldehyde, with high selectivity under mild conditions, even at room temperature[6, 12]. Nevertheless, its practical application remains constrained by several intrinsic challenges, such as slow mass transfer, limited light-harvesting capability, and rapid charge carrier recombination[16–18]. These limitations result in low methane conversion rates (typically 10–100 times lower than those

Received: September 24, 2025; **Revised:** January 13, 2026
Accepted: January 29, 2026

✉Address correspondence to uceclii@ucl.ac.uk; yang.lan@ucl.ac.uk

https://doi.org/10.26599/CF.2026.9200067

achieved via thermocatalysis) and poor quantum efficiencies (generally < 20%)[6, 19].

In recent years, photo-thermo synergistic catalysis has emerged as a next-generation platform for methane activation, integrating the complementary advantages of both photocatalysis and thermocatalysis (Fig. 1). This dual-energy approach effectively addresses the limitations associated with single-energy driving forces[20–22]. Briefly, it enables the use of photons to overcome high activation barriers, such as C–H bond cleavage and oxidant activation, while simultaneously harnessing phonons to accelerate key elementary steps including mass and charge transfer, intermediates migration, and bond reconstruction. Despite its promising potential, the application of photo-thermo synergistic catalysis in direct methane conversion remains in its early stages. Several methane conversion processes, such as steam reforming of methane (SRM)[23, 24], dry reforming of methane (DRM)[25, 26], partial oxidation of methane (POM)[27, 28] and oxidative/non-oxidative coupling of methane (OCM/NOCM)[29, 30], have been successfully implemented using photo-thermo synergistic mechanisms. These approaches have yielded a wide range of valuable products from C_1 to C_3 compounds, including syngas (CO/H_2), C_1 (methanol, formaldehyde, formic acid), C_2 (ethylene/ethane, ethanol, acetic acid), and C_3 (propane) products, thereby significantly enriching the methane conversion landscape. Notably, these strategies have shown significantly enhanced reactivity, often achieving yields several to dozens of times higher than conventional photocatalysis, while maintaining high selectivity (typically > 90%) and excellent stability over extended durations (ranging from tens to hundreds of hours) compared to conventional thermocatalysis. A variety of multifunctional catalysts tailored to different reaction environments have been explored. Four distinct modes of photo-thermo synergistic catalysis have been identified. The associated photophysics and surface chemistry have also been elucidated in the new systems.

This review seeks to deliver a timely and comprehensive overview of photo-thermo catalytic methane conversion. We begin by elucidating the fundamental principles underlying the synergistic interactions between photon and phonon. Next, we summarise recent advances in catalyst design and reaction system engineering, with particular emphasis on the roles of photo and thermal energy in enhancing selectivity and accelerating yields of C_1–C_3 desired products. Finally, we highlight the key challenges that remain in this emerging field and offer perspectives on future directions, including performance benchmarking, broadening the product scope, real-time mechanistic investigations, reactor design, and AI-driven catalyst discovery.

2 Types of photo-thermo synergistic catalysis

The complex interplay between photo and thermal stimuli in photo-thermo catalytic methane conversion systems necessitates a clear classification to advance mechanistic understanding and guide material design and reaction system engineering. The synergistic photo-thermo effects in methane conversion can be categorised into four distinct modes: thermo-assisted photocatalysis, photo-enhanced thermocatalysis, photo-thermo cascade catalysis, and photo-to-thermo catalysis, as shown in Fig. 2. In certain cases, multiple mechanisms may coexist within a single reaction system. This framework clarifies the distinct roles of photon and phonon, providing a robust foundation for investigating and optimising catalytic performance in methane conversion processes.

2.1 Thermo-assisted photocatalysis

Thermo-assisted photocatalysis refers to a process in which light serves as the primary driving force for the reaction, while thermal energy plays a supportive role in enhancing efficiency. This process typically occurs at relatively low temperatures (< 250 °C) and cannot be driven solely by thermal energy due to the high kinetic or thermodynamic barriers. The introduction of photons can overcome these barriers, facilitating a thermodynamically favourable "downhill" reaction[21]. In this mechanism, the

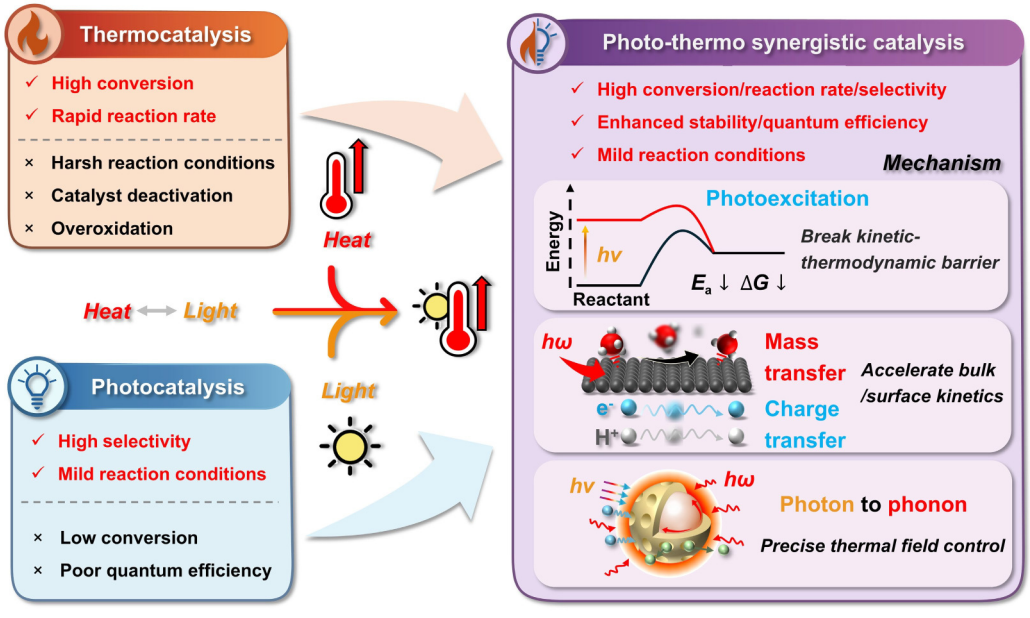

Fig. 1. Thermocatalytic, photocatalytic and photo-thermo catalytic direct methane conversion.

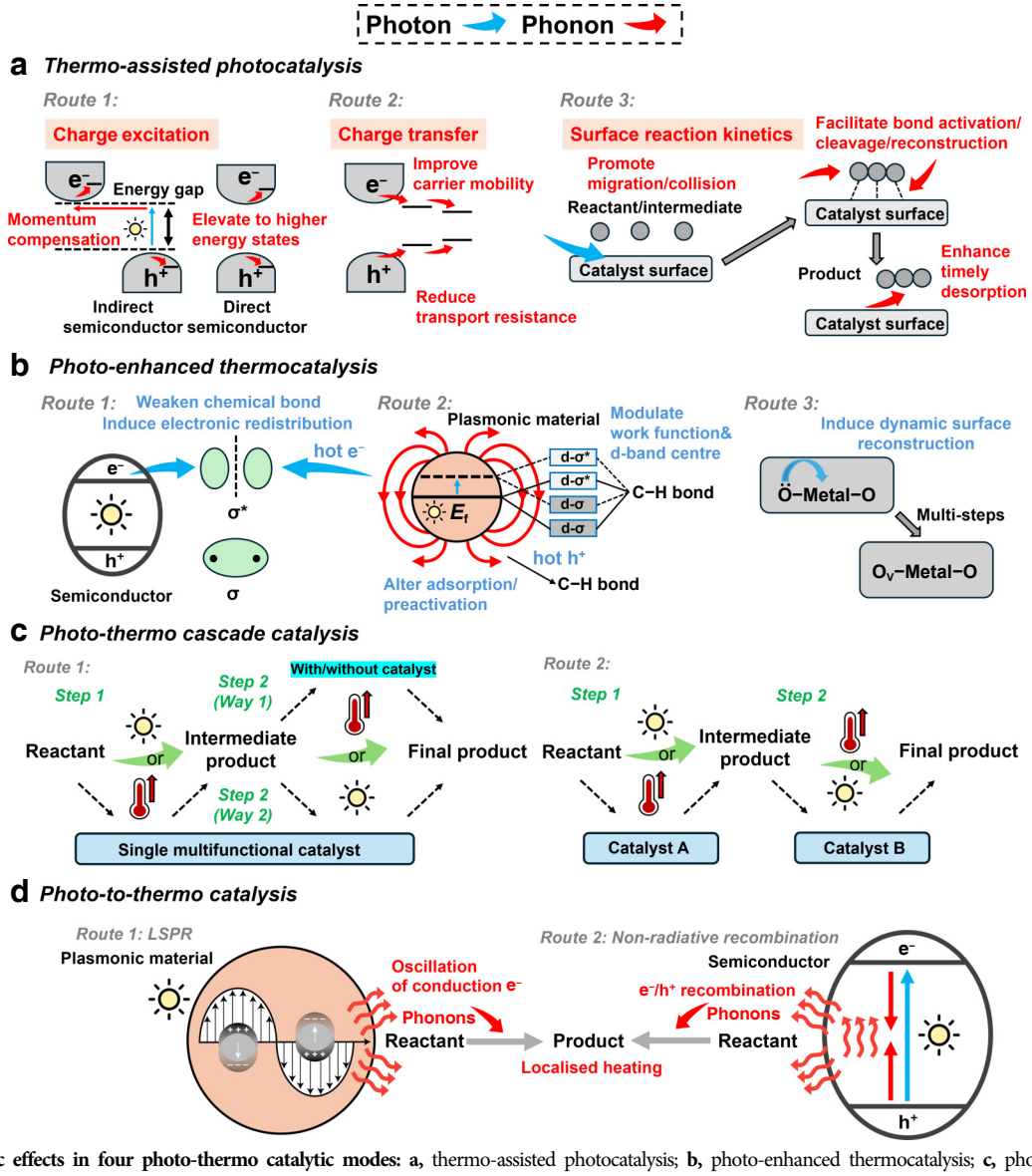

Fig. 2. Synergistic effects in four photo-thermo catalytic modes: a, thermo-assisted photocatalysis; **b,** photo-enhanced thermocatalysis; **c,** photo-thermo cascade catalysis; **d,** photo-to-thermo catalysis.

photocatalytic component absorbs photons with energy (on the order of a few eV) equal to or greater than its bandgap, exciting electrons to the conduction band and leaving holes in the valence band[6, 31]. While some photogenerated electron-hole pairs may recombine, the remaining charge carriers migrate to the surface, where they drive the activation of substrate molecules (e.g., CH_4, H_2O, O_2, and H_2O_2). Thermal energy can contribute to three fundamental steps (Fig. 2a): 1) charge excitation: for indirect semiconductors, thermal energy (phonons) compensates for momentum mismatch during light-induced electronic transitions from the valence band to the conduction band, enhancing electron excitation efficiency[32]. Additionally, thermal energy can elevate electrons to higher energy states, increasing their driving force in specific cases[33, 34]. 2) charge transfer: thermal energy facilitates the release and hopping of charge carriers between discrete localized states, improving carrier mobility, reducing transport resistance, and enabling efficient surface charge accumulation for reactions[35, 36]. 3) surface reaction kinetics: thermal energy (0.1–1 eV) accelerates surface elementary steps by enhancing the migration and collision frequency of reactants and intermediates, aiding bond activation, cleavage and reconstruction, and promoting the timely desorption of products[6, 12, 17, 22, 31, 37, 38].

In methane conversion, thermo-assisted photocatalysis has proven particularly effective for reactions such as POM, NOCM, and OCM, where precise control over the partial dehydrogenation of CH_4 is often critical. In this synergistic approach, C–H activation is primarily achieved by the photocatalytic component, either through photohole abstraction or reactive oxidative species such as ·OH cleavage. Both mechanisms require a valence band with sufficiently positive potential; thus, oxide semiconductors like TiO_2, ZnO, and CeO_2 are commonly employed due to their O 2p orbitals derived valence bands[27, 29, 30], which can reach potentials as high as ~ 3 V vs. NHE[39]. To further enhance activity and selectivity, noble metals such as Au, Pd, and Pt and their derivatives (e.g., alloys) are frequently integrated with the semiconductor matrix. These metals contribute through different aspects, including C–H bond preactivation, facilitation of charge transfer, regulation of oxygen-containing radicals, and tuning of redox potentials[30, 40–42]. The

desired products often result from the recombination of two or more radical species (e.g., CH_3· + CH_3·, CH_3· + ·OH). Therefore, mild thermal input from an external source is typically applied to the entire reaction system to facilitate this process on the catalyst surface or reaction environment, rather than being targeted at a dedicated thermocatalytic component. Moreover, emerging systems are incorporating absorptive materials to harness low-energy, long-wavelength photons for localised thermal generation[43]. Examples include surface plasmonic metals and carbon-based materials, which enable efficient utilisation of solar spectrum and contribute to the thermal enhancement of photocatalytic processes[28, 44].

2.2 Photo-enhanced thermocatalysis

Photo-enhanced thermocatalysis refers to a process where thermal energy serves as the primary driving force, enabling reactions even under dark conditions (typically at elevated temperatures > 300 °C), while light plays a promotional role in enhancing selectivity, stability, or energy efficiency. In such systems, light alone is insufficient to drive the reaction. For instance, in the DRM reaction, the reduction potential required for CO_2 activation could be low to −1.9 V versus normal hydrogen electrode (NHE), while the oxidation potential for CH_4 oxidation is around +1.7 V versus NHE[45, 46]. This results in a minimum bandgap requirement of 3.6 eV, which exceeds the capabilities of most common semiconductors[47], rendering direct photocatalytic activation challenging.

The thermocatalytic component in this mechanism involves five classical sequential steps: reactant adsorption, bond activation, intermediates formation, products formation, and products desorption[48]. Each step has distinct energy barriers, with the overall reaction rate typically governed by the step with the highest activation energy (E_a). In conventional thermocatalysis, thermal energy alone overcomes these barriers. In contrast, photo-enhanced thermocatalysis leverages photon excitation to contribute in three key ways (Fig. 2b): 1) photoelectrons/photoholes generated from the semiconductor component can be injected into the antibonding orbitals of reactant molecules[24, 31], facilitating targeted bond weakening and electronic redistribution, thereby lowering the energy barriers of critical reaction steps[24]. 2) metallic components exhibiting localised surface plasmon resonance (LSPR) effects can not only donate the active hot carriers to activate the substrates, similar to conventional photocarriers, but also modulate metal nanoparticles' work function and d-band centre through hot charge accumulation[24, 49, 50]. This alters the adsorption and preactivation behaviour of substrate molecules, enhancing catalytic efficiency. 3) in certain cases, photogenerated charge carriers can induce dynamic surface reconstruction, such as increasing the concentration of oxygen vacancies[51–53], which enriches active sites and enhances catalytic performance.

This photo-thermo synergistic mode is mainly employed in SRM and DRM reactions. A key reason for its effectiveness in these reactions is that the desired products, CO and H_2, are the result of complete dehydrogenation of CH_4. This allows for the application of elevated temperatures to meet both kinetic and thermodynamic requirements without the risk of overreaction or undesired side products. Since thermal energy also contributes significantly to C–H bond activation in these systems, the band position of the photocatalytic component is less critical compared to thermo-assisted photocatalysis, which relies more heavily on photocatalytic C–H activation. Consequently, the range of suitable catalysts is not limited to metal oxide semiconductors. Catalyst design in this context is primarily inspired by thermocatalysis, with metals known for their strong C–H cleavage capabilities, such as Ni, Rh, and Ru, being particularly favoured[54]. To harness the energetic carriers generated by photon excitation, these metals are often integrated with semiconductors (e.g., CeO_2, TiN, and $SrTiO_3$) or plasmonic metals (e.g., Au and Cu) through strategies such as surface decoration, alloying, or lattice substitution[25, 55–57]. Recently, high-entropy materials have emerged as a versatile platform for tailoring catalytic properties and assembling multifunctional components. This includes the development of high-entropy alloy catalytic centres (e.g., CoNiRuRhPd) and high-entropy oxide supports (e.g., $CoNiFeZnCrO_x$)[58, 59]. Despite these innovations, it is evident that the most effective catalytic components remain largely unchanged, underscoring the enduring relevance of well-established active sites in methane reforming reactions.

2.3 Photo-thermo cascade catalysis

Photo-thermo cascade catalysis represents a novel synergistic mode in which photocatalysis and thermocatalysis are temporally and/or spatially separated, enabling a stepwise mechanism where photon and phonon independently drive distinct elementary steps. In this process, reactants are first converted into intermediate products via either light- or thermo-driven step, followed by their transformation into final products under a different energy input. Unlike the transient intermediates in thermo-assisted photocatalysis and photo-enhanced thermocatalysis, which rapidly convert to final products within a single reaction step, photo-thermo cascade catalysis generates intermediate species that can accumulate or persist until the second energy input is applied. This catalytic mode can be broadly categorised into two types (Fig. 2c): 1) a single catalyst system in which both photo- and thermo-driven steps occur by varying the energy input[27]. 2) a dual-component system comprising two distinct catalytic materials, one activated by photons and the other by phonons, where intermediates generated on one catalyst are subsequently transformed on the other[38]. The fundamental mechanisms of the photocatalytic and thermocatalytic components align with those discussed in Sections 2.1 and 2.2.

Although photo-thermo cascade catalysis presents an ideal platform for designing diverse reaction pathways, enabling precise control over intermediate formation and directional conversion, it remains significantly underexplored. To date, only two applications of photo-thermo cascade catalysis have been reported, both related to POM with formaldehyde and formic acid as products, respectively[27, 60]. These reactions were initiated by photon-driven C–H activation; therefore, typical metal oxide semiconductors such as ZnO and TiO_2 were employed as the primary photocatalytic base due to their strong oxidative potential, as discussed in Section 2.1. Interestingly, a dedicated thermocatalytic component is not always required to achieve sequential transformation; in some cases, intermediates can undergo spontaneous conversion with the input of thermal energy[27]. Notably, there are no reported examples of photo-thermo cascade catalysis initiated via thermocatalytic C–H activation. This may be attributed to the inherent challenge of controlling reactive intermediates, as many products derived from CH_4 conversion are more reactive than CH_4 itself, making it difficult to arrest the reaction at intermediate stages[12]. To overcome this limitation, spatially separated cascade catalytic systems, constructed by assembling two distinct functional units, may offer a promising alternative to conventional multicomponent catalyst design.

2.4 Photo-to-thermo catalysis

Photo-to-thermo catalysis converts light energy into thermal energy to drive thermocatalytic reactions without external heating. Localised heat is generated via two primary photons-to-phonons pathways (Fig. 2d): LSPR and non-radiative recombination of charge carriers in semiconductors. In LSPR, metallic nanostructures undergo collective oscillation of conduction electrons under light irradiation, concentrating electromagnetic energy at the surface. This energy is subsequently converted into heat via a series of non-radiative processes, such as Landau damping, electron-electron scattering, electron-phonon coupling, and phonon-phonon interactions[22, 61–63]. On the other hand, in semiconductors with narrow bandgaps, photogenerated electrons and holes release electronic energy as lattice vibrations (phonons) during relaxation to lower energy states and recombination, serving as a localised heat source[20].

In contrast to conventional thermocatalysis, which relies on external heating to achieve relatively uniform bulk temperatures, the photo-to-thermo catalytic pathway delivers energy directly to optically active nanoscale domains[31, 38]. This approach enables precise, site-specific, and energy-efficient heating, minimising energy losses to non-catalytic components (e.g., reactor walls). Moreover, localised heating can also generate vertical temperature gradients across catalyst layers and interfaces through subtle manipulation, creating tailored microenvironments that address the distinct kinetic and thermodynamic requirements of individual elementary reaction steps[64]. This capability mitigates conflicting temperature demands at the nanoscale, thereby enhancing the overall efficiency of the catalytic process. By harnessing the full solar spectrum, photo-to-thermo catalysis offers a sustainable alternative to fossil fuel-based energy inputs.

Since the intrinsic nature of this mode as thermocatalysis, high temperatures, comparable to those used in conventional thermocatalysis, are required for effective CH_4 activation. As discussed in Section 2.2, DRM is particularly well-suited to this approach. Materials with superior light absorption capabilities, encompassing both broad spectral responsiveness and high absorption efficiency, are ideal supports for assembling with thermocatalysts. Carbon-based materials, such as carbides, are especially promising due to their extremely narrow bandgaps and responsiveness extending into the infrared region[65]. However, when both photocatalysis and photo-to-thermo catalysis are involved at the same time under light irradiation, the resulting enhancement in thermodynamic efficiency in DRM surpasses that achieved through photo-to-thermo catalysis alone[43]. Consequently, this mode is more commonly integrated with other catalytic strategies rather than employed in isolation. Many catalysts have thus been developed based on plasmonic metals, such as NiCu and RuCu, leveraging the dual functionality of Cu as a contributor to both thermal energy and hot carrier generation[56, 66]. It is important to clarify that photo-to-thermo catalysis is distinct from the photo-to-thermo effect. The key difference lies in their functional roles: photo-to-thermo catalysis refers to a process in which thermal energy generated from photon absorption can drive the chemical reaction without the need for coupling with other catalytic modes. In contrast, the photo-to-thermo effect can occur more broadly across various systems and does not necessarily initiate or sustain a reaction on its own. Instead, it often serves to enhance existing processes, such as accelerating migration and desorption kinetics.

3 Photo-thermo catalytic methane conversion

Photo-thermo synergistic catalysis has enabled the production of diverse products in recent years, driven by the development of multifunctional catalysts and co-catalysts integrated into innovative reaction systems. These systems show superior performance compared to processes driven by a single energy source. This review focuses on representative methane conversion products, elucidating the complementary roles of light and heat in these processes. By providing a comprehensive overview of recent advancements, we aim to highlight the transformative potential of photo-thermo catalysis in sustainable methane valorisation.

3.1 Methane to C_1 chemicals

3.1.1 Methanol

The conversion of methane (CH_4) to methanol (CH_3OH) requires the incorporation of an additional oxygen atom, typically sourced from O_2, H_2O, or H_2O_2, necessitating the co-activation of CH_4 and oxygen-containing reactants. In conventional thermocatalysis, H_2O_2 is often used as an oxygen source due to its controllable reactivity, but its high cost exceeds that of methanol itself[67]. Using O_2 as the oxidant at elevated temperatures risks overoxidation, as reactive oxide radicals may form randomly and CH_3OH is more reactive than CH_4[12]. The high bond energy of H_2O (O–H, ~ 492 kJ·mol^{-1})[68] demands high temperatures for activation, often leading to deep dehydrogenation of CH_4 and significant energy consumption[69]. In contrast, photocatalysis enables precise activation of O_2 and H_2O to generate specific oxygen-containing radicals through tailored band structure design[47, 70], as shown in **Fig. 3**a. Consequently, thermo-assisted photocatalysis, where the photocatalytic component serves as the main driver, is widely employed for methane-to-methanol conversion. In particular, photoexcitation can also facilitate C–H bond activation under mild conditions through generating active species, such as photohole[71] and ·OH radical[28, 72, 73]. Thermal energy promotes the kinetics of some surface reactions, such as the collision of CH_3· and ·OH radicals, timely CH_3OH desorption[28, 73], further improving CH_3OH yield compared to photocatalysis alone.

A notable example of thermo-assisted photocatalysis is shown by a single atom Au/black phosphorus (BP) catalyst operating in aqueous media under visible light irradiation at 90 °C[73]. In this system, BP functioned as the photocatalytic component, generating photoelectron and photohole pairs. Photoelectrons reduced O_2 to superoxide radicals, which recombined with photoholes to form singlet O_2. Singlet O_2 then reacted with water to produce surface hydroxyl groups and ·OH radicals. The hydroxyl groups activated C–H bond of methane to form CH_3*, which further reacted with ·OH to yield CH_3OH. Throughout this process, thermal energy at 90 °C overcame residual barriers, accelerating each reaction step and, crucially, facilitating CH_3OH desorption to achieve > 99% CH_3OH selectivity.

Although thermal energy may not always directly drive reaction steps, its indirect contributions, such as enhanced substrate diffusion, significantly boost production rates, as shown by the Pd_1FeO_x/aUiO(H) catalyst[28]. This catalyst employed a metal-organic framework (MOF) decorated with atomically dispersed Pd and Fe sites to construct a photocatalytic nanoreactor. In this system, photoelectrons reacted with O_2 and H_2O to generate H_2O_2 *in-situ* at the Pd sites. The H_2O_2 subsequently oxidised Fe sites to

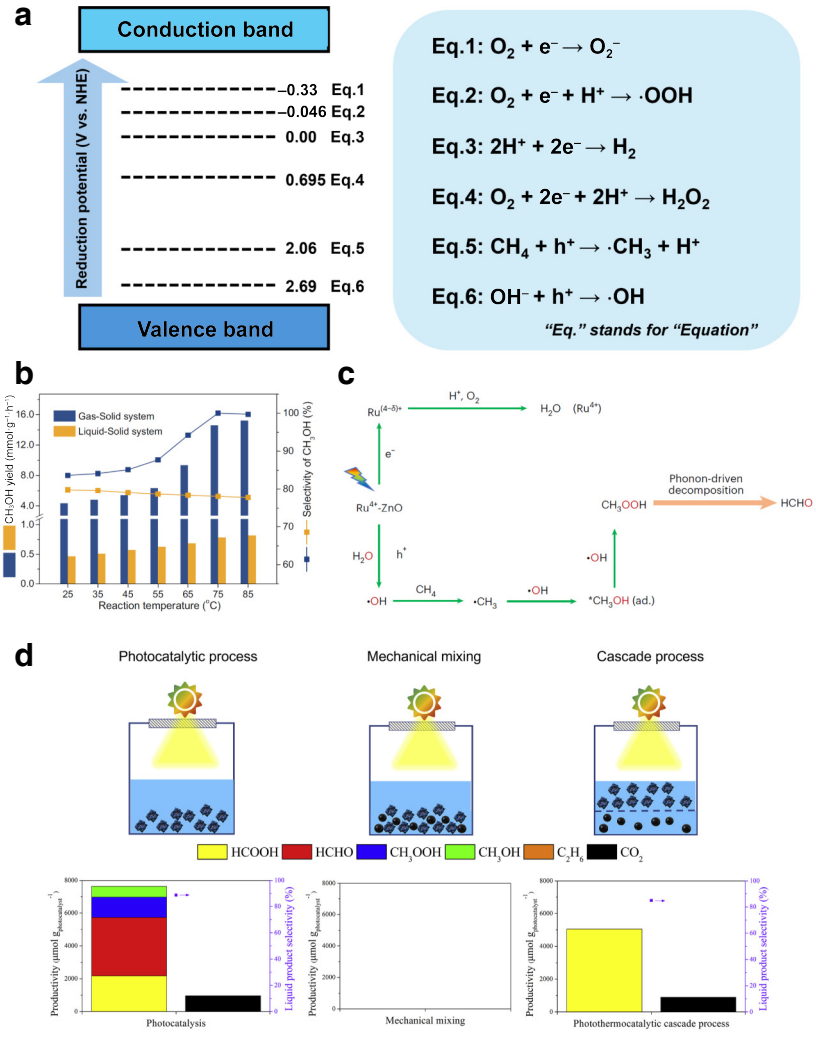

Fig. 3. Photo-thermo catalytic methane conversion to C_1 oxygenates. a, Redox potentials relevant to methane activation and the generation of active oxygen-containing species. **b,** CH_3OH yield and selectivity on Pd_1FeOx/aUiO(H) catalyst at different temperatures. Reproduced with permission from Ref.[28], © Hao, Y. et al. 2025. **c,** Mechanism of photo-thermo cascade catalysis for methane oxidation to formaldehyde over the Ru-ZnO catalyst. Reproduced with permission from Ref.[27], © Xu, Y. et al. 2024. **d,** Different assembly modes of CsPW-TiO_2 and Ru/Al_2O_3 catalysts for methane oxidation. Reproduced with permission from Ref.[60], © Elsevier Ltd. 2023.

Fe^{IV}=O species, releasing ·OH radicals. CH_3·, generated via homolytic C–H bond cleavage by Fe^{IV}=O, then recombined with ·OH radicals to yield CH_3OH. Unfortunately, under ambient conditions (25 °C), water vapour tended to accumulate within the MOF pores, severely hindering the diffusion of other reactants (e.g., O_2 and CH_4) and diluting the concentration of the crucial H_2O_2 intermediate. Interestingly, thermal energy could play a pivotal role in interfacial water management. By increasing the reaction temperature to 75 °C, water uptake was reduced by approximately sixfold, thereby minimising water retention and enhancing the diffusion of reactants and timely desorption of products. As shown in Fig. 3b, this temperature increase led to a nearly three-fold enhancement in methanol yield, while selectivity improved from 85% to 100%. To eliminate the need for external heating while maintaining elevated reaction temperatures, a carbon-based gas diffusion layer was integrated to form a hybrid MOF membrane. This design harnesses infrared light from the solar spectrum to initiate a photo-to-thermo pathway, while reserving UV–Vis light for the photocatalytic components. As a result, this system was successfully operated under outdoor sunlight in an unusual thermo-assisted photocatalysis process without any additional energy input.

In addition, photo-enhanced thermocatalysis has also been reported as an alternative synergistic mechanism for methanol synthesis[74, 75]. For instance, a dual-functional Cu-MOR/g-C_3N_4 catalyst was designed, in which Cu species were responsible for the thermocatalytic activation of methane, while g-C_3N_4 facilitated the photocatalytic regeneration of active Cu sites. During the reaction, thermally activated Cu_xO_y species, formed via O_2 activation at 200 °C, enabled methane conversion to CH_3OH. However, the reduced Cu_xO_{y-1} species required reoxidation by O_2 to restore catalytic activity, a step that limited overall efficiency. The incorporation of g-C_3N_4 addressed this bottleneck by accelerating the regeneration of active Cu sties. Specially, photoelectrons from g-C_3N_4 reacted with O_2 to generate superoxide radicals, which promoted the reoxidation of Cu_xO_{y-1} back to Cu_xO_y. This indirect photocatalytic assistance led to a 25.9% increase in CH_3OH yield. This photocatalytic component did not directly activate methane but instead sustained the catalytic cycle, which enriches the mechanistic landscape of methane-to-methanol conversion.

3.1.2 Formaldehyde

Apart from CH_3OH, formaldehyde (HCHO) is another widely studied oxygenate produced via direct methane conversion[76]. Achieving HCHO formation requires further dehydrogenation (oxidation) for the carbon atom compared to CH_3OH, with a change in oxidation state from −2 to 0. Consequently, controlling selectivity in the direct conversion of methane to formaldehyde is particularly challenging due to the sequential oxidation steps and the tendency toward overoxidation to the thermodynamically stable overoxidation product, CO_2 ($CH_4 \rightarrow CH_3OH \rightarrow HCHO \rightarrow CO_2$)[70, 77]. In this case, photocatalysis is generally more suitable than thermocatalysis as the dominant driving force for methane activation, owing to its superior ability to modulate oxidation extent, as discussed in section 3.1.1. To date, two distinct pathways for methane oxidation to formaldehyde have been reported in photo-thermo synergistic catalysis[27, 78, 79]: 1) a stepwise oxidation process via CH_3OH intermediates, and 2) a direct one-step oxidation to HCHO.

In the first pathway, the photocatalytic components in photo-thermo catalysis operated similarly to conventional photocatalysis, generating a series of radicals or intermediates (e.g., CH_3OOH, CH_2OH, and $OHCH_2OH$) through the action of photoelectrons and photoholes in the presence of H_2O, O_2 and even H_2O_2[77, 80–82]. Several studies (e.g., WO_3 and Pd_8Sb_3) have shown that the introduction of moderate thermal energy, either via external heating or *in-situ* LSPR heating to achieve a thermo-assisted photocatalysis mode, can enhance HCHO yield by accelerating general kinetic steps such as mass transfer and diffusion[78, 83].

In contrast, a more targeted approach focusing on the key intermediate CH_3OOH has enabled a unique photo-thermo cascade catalysis strategy, achieving unprecedented HCHO yield with high selectivity over a Ru single atom decorated ZnO catalyst[27] (Fig. 3c). It was found that CH_3OOH remained stable at 30 °C for extended periods, while thermal treatment at 150 °C under dark conditions could convert it to formaldehyde with ~ 80% selectivity. This intermediate thus served as a bridge between two distinct energy-driven processes. Initially, CH_3OOH was formed via a general photocatalytic pathway: photoholes oxidised H_2O to ·OH, which abstracted hydrogen from methane to form CH_3·. The resulting CH_3· coupled with ·OH to yield adsorbed CH_3OH*, which was further oxidised by ·OH to produce CH_3OOH. Subsequently, the co-presence of thermal energy drove the conversion of CH_3OOH to HCHO. This complete cascade process, combining photon and phonon inputs (365 nm light and 150 °C heating), achieved a formaldehyde production rate of 401.5 μmol·h^{-1} with 90.4% selectivity. This new photo-thermo synergistic strategy represented a significant advancement, delivering nearly an order-of-magnitude improvement in formaldehyde production rate compared to previous photocatalytic systems. Moreover, the methane conversion rate matched that of thermocatalytic processes operated above 500 °C, while maintaining substantially higher formaldehyde selectivity (> 90% vs. < 65%).

Recently, the second pathway (direct one-step oxidation of methane to formaldehyde) has also been observed via a thermo-assisted photocatalytic process[79]. Unlike the first pathway, which involved a variety of oxygen-containing radicals, this mechanism utilised lattice oxygen from ZnO as the oxygen source HCHO formation, following a Mars-van Krevelen cycle. Under light irradiation, single-atom Ag sites served as photohole acceptors on ZnO, initiating hydrogen abstraction from methane to form surface-bound *CH_2 species. Thermal input (surface temperature ~ 228°C), in conjunction with the Ag single atom, enhanced lattice oxygen activation, enabling its reaction with *CH_2 and desorb HCHO. Meanwhile, photoelectrons reduced O_2 to replenish the consumed lattice oxygen, thereby completing the catalytic cycle. The critical role of thermal assistance was evidenced by a dramatic enhancement in formaldehyde production rate, over 50-fold compared to room temperature conditions. Notably, this system achieved a record-high formaldehyde concentration (~ 1.5%) among all reported photocatalytic systems, showing strong potential for synthesising industrial-grade HCHO solutions via photo-thermo synergistic catalysis.

3.1.3 Formic acid

Compared with the direct conversion of methane to methanol/formaldehyde in Section 3.1.1 and 3.1.2, formic acid (HCOOH) through photo-thermo synergistic catalysis remains relatively underexplored. Its high oxidation states (close to CO_2) results in the challenge control in selectivity may be one of the reasons[84]. Given the slow progress in this field, it is reasonable to see that the mechanism, in particular the main role of photons and phonons, has not been fully understood in-depth. For example, a TiO_2-HSiMo interface was constructed to efficiently convert methane to formic acid via thermo-assisted photocatalysis[85]. Although the mechanism of photocatalytic component has been well discussed in detail, such as the C–H/O–H activation by photoholes, the precise role of thermal input remained unclear, despite a nearly tenfold increase in formic acid yield when the temperature was raised from 50 °C to 150 °C.

Surprisingly, another example of photo-thermo cascade catalysis has recently emerged in methane conversion to formic acid—an especially rare and valuable development in the field of photo-thermo synergistic catalysis[60]. Given that both HCHO and HCOOH are stepwise oxidation products, it is perhaps reasonable that this catalytic mode would appear in their formation reactions. Unlike the Ru/ZnO system for HCHO production discussed in Section 3.1.2, which achieved cascade catalysis through manipulation of reaction conditions, this study employed two distinct catalytic components: a photocatalyst (CsPW-TiO_2) and a thermocatalyst (Ru/Al_2O_3), designed to operate synergistically. As shown in Fig. 3d, CsPW-TiO_2 alone produced a broad range of oxygenates, such as HCOOH, HCHO, CH_3OH alongside CO_2, due to the inherent difficulty in controlling selectivity within such a complex oxidation network. Meanwhile, Ru/Al_2O_3, capable of converting CH_3OH and HCHO to HCOOH under thermocatalytic conditions, showed limited activity when physically mixed with CsPW-TiO_2. This was likely because of light-blocking effects that hindered photocatalytic activation process. To overcome this, a tandem reactor configuration was implemented using a sand filter to spatially separate the two catalysts: CsPW-TiO_2 was placed in the top layer to receive light irradiation, while Ru/Al_2O_3 was positioned below. This design enabled sequential reaction steps in distinct microenvironments. Remarkably, the production of formic acid was significantly enhanced compared to the single-photocatalyst system, achieving a high selectivity of 85%. This dual catalyst, dual reaction microenvironment strategy represents a significant advancement in the application of photo-thermo cascade catalysis. It not only shows the feasibility of spatially and temporally decoupling reaction steps but also provides a valuable blueprint for designing future systems aimed at producing other selective oxidation products.

Table 1 summarizes representative advances in the photo-thermo catalytic conversion of methane to C_1 oxygenates (CH_3OH, HCHO, and HCOOH). Thermo-assisted photocatalysis remains the dominant synergistic approach, accounting for most reported systems, while photo-enhanced thermocatalysis and photo-thermo cascade catalysis have only emerged as complementary strategies. A strong reliance on noble metals (Pd, Ru, Au, and Ag) is evident, as these systems consistently outperform non-noble metal catalysts in productivity. For instance, Cu-based catalysts exhibit only moderate CH_3OH production rate compared to noble-metal systems, which can achieve rates even more than two orders of magnitude higher, even under milder conditions. This highlights a critical need for developing low-cost materials to break the trader-off between activity and price. Most studies have been conducted in batch reactors, which are suitable for initial catalyst screening but impractical for scale-up. Continuous flow systems are essential to advance these reactions toward industrial application. Regarding product performance, CH_3OH and HCHO can achieve near 100% selectivity and higher production rate, reflecting their kinetic favourability as primary oxidation products. In contrast, HCOOH is limited by the inherent kinetic challenges of multi-step oxidation and thermodynamic constraints associated with deeper oxidation, where CO_2 represents the most stable product. Furthermore, despite frequent claims of record-high production rate or performance comparable to thermocatalysis, CH_4 conversion, a critical metric in catalysis, is often overlooked. Many batch reactions operate under high CH_4 pressures to enhance reactant solubility in water, yet conversions remain low. For example, Ru/ZnO achieved the highest reported production rate (401.5 μmol·h^{-1}) but only 1.1% CH_4 conversion at 20 bar[27]. Such low conversion poses significant challenges, including reactant waste, increased separation costs for products, and more importantly, potential selectivity issues at higher conversions as all C_1 products are more reactive than CH_4 itself. Collectively, these findings indicate that integrating photo-thermo synergistic effects offers clear improvements over pure photocatalytic processes in CH_4 conversion to C_1 products. However, substantial progress is still required before these systems can deliver practical catalytic performance across all key metrics.

3.2 Methane to C_2 chemicals

3.2.1 *Ethylene/Ethane*

The direct conversion of methane to ethane (C_2H_6) and/or ethylene (C_2H_4) proceeds via two pathways: OCM and NOCM. A critical step in both processes is C–C bond formation, exemplified by the coupling of two CH_3· radicals to form ethane. Thermocatalytic OCM and NOCM typically require very high temperatures (> 600 °C), making precise control over dehydrogenation (oxidation) to CH_3·/CH_2· intermediates particularly challenging. This difficulty arises from the comparable activation barriers of sequential dehydrogenations steps and the strong thermodynamic preference for stable byproducts (CO_2 under aerobic conditions and coke under anaerobic conditions)[10, 12, 38, 88, 89]. In contrast, photocatalysis enables more controlled C–H activation under mild conditions by employing photogenerated redox carriers to selectively produce intermediates such as CH_3·[6, 12]. Notably, photocatalysis can even overcome thermodynamic equilibrium constraints in NOCM, achieving yield improvements of 100 to 10000 times at room temperature[6, 12]. Consequently, the photocatalytic component often plays a dominant role in photo-thermo synergistic catalysis for methane coupling. A closer examination of photocatalytic methane coupling reveals that, following photon activation, the migration of CH_3· to recombine with another CH_3· is a fundamental step. This process may involve

Table 1 Representative examples of photo-thermo conversion of CH_4 to C_1 oxygenates

Catalyst	Photo-thermo synergistic type	Reaction conditions	Production rate (μmol·h^{-1})	Selectivity (%)	Ref.
Pd_1FeO_x/aUiO(H)	Thermo-assisted photocatalysis	Batch reactor, 50 mg catalyst, simulated sunlight, 75 °C	CH_3OH: 730	CH_3OH: ~ 100	[28]
Bi_2S_3/BiOCl	Thermo-assisted photocatalysis	Batch reactor, 10 mg catalyst, 320–1100 nm, ~ 500 mW·cm^{-2}, 67.2 °C	CH_3OH: 59.15	CH_3OH: 90.2	[86]
Cu/p-GaN	Thermo-assisted photocatalysis	Flow reactor, 0.28 mg catalyst, full spectrum, 5000 mW·cm^{-2}, 212 °C	CH_3OH: 3.584	CH_3OH: 23	[87]
Au/BP	Thermo-assisted photocatalysis	Batch reactor, 200 mg catalyst, full spectrum, 382 mW·cm^{-2}, 90 °C	CH_3OH: 11.35	CH_3OH: > 99	[73]
Cu/Ti-ZSM-5	Photo-enhanced thermocatalysis	Flow reactor, 100 mg catalyst, 200–400 nm, 360 mW·cm^{-2}, 300 °C	CH_3OH: 6.741	CH_3OH: 92	[75]
Cu-MOR/g-C_3N_4	Photo-enhanced thermocatalysis	Flow reactor, 100 mg catalyst, > 420 nm, 500 °C	CH_3OH: 0.309	/	[74]
Ag-ZnO	Thermo-assisted photocatalysis	Flow reactor, 4 mg catalyst, 200–1200 nm light, 1000 mW·cm^{-2}, 228 °C	HCHO: 117.8	HCHO: 71.2	[79]
Pd_8Sb_3	Thermo-assisted photocatalysis	Batch reactor, 0.4 mg catalyst, 300–2500 nm light, 1700 mW·cm^{-2}, 70 °C	HCHO: 133	HCHO: 98.7	[78]
WO_3	Thermo-assisted photocatalysis	Batch reactor, 10 mg catalyst, 300–700nm light, 150 mW·cm^{-2}, 50 °C	HCHO: 1.65	HCHO: ~100	[83]
Ru-ZnO	Photo-thermo cascade catalysis	Batch reactor, 10 mg catalyst, 365 nm LED, 75 mW·cm^{-2}, 150 °C	HCHO: 401.5	HCHO: 90.4	[27]
HSiMo/TiO_2	Thermo-assisted photocatalysis	Batch reactor, 20 mg catalyst, simulated sunlight, 150 °C	HCOOH: 13.59	HCOOH: 45	[85]
CsPW-TiO_2 and Ru/Al_2O_3	Photo-thermo cascade catalysis	Batch reactor, 10 mg CsPW-TiO_2 catalyst and 1 g Ru/Al_2O_3 catalyst, full spectrum	HCOOH: 25.28	HCOOH: 85	[60]

several energy-uphill transitions[88], suggesting that phonon participation can enhance overall activity. Furthermore, timely desorption of the formed products is essential to prevent further dehydrogenation and overoxidation during the photocatalytic cycle. Thermal input is expected to facilitate this step, thereby improving selectivity and mitigating coke formation[40, 44, 88, 90, 91].

In recent years, numerous thermo-assisted photocatalytic OCM systems have been developed, such as Au/TiO_2[30], Au-ZnO/TiO_2[88], Au/CeO_2[29], and Au/CeO_2/ZnO[44], all showing significant enhancements in ethane yield, ranging from several tens to over 200% as the reaction temperature increased from 40–70 °C to 120–170 °C. Among these, Au/CeO_2/ZnO has been systematically investigated as a model catalyst to elucidate the role of thermal energy[44]. In this system, Au nanoparticles exhibited LSPR effect, generating *in-situ* thermal fields under full solar irradiation that promote the reaction. To isolate the influence of photo-to-thermo effects, a low-intensity monochromatic light source (360 nm) was used during thermal effect studies (**Fig. 4a**). Ethane production rates increased with temperature up to ~ 200 °C, beyond which a decline was observed, likely due to reduced reactant adsorption orenhanced charge carriers recombination, as previously reported[6, 92, 93]. Notably, the apparent quantum efficiency (AQE), which reflects photon utilisation efficiency, nearly double as the temperature increased from 80 to 200 °C. To further investigate the underlying mechanism, DFT simulations were performed to quantify energy barriers for key reaction steps at different temperatures (Fig. 4b). Interestingly, while the barrier for CH_4 dissociation remained unaffected by temperature, the desorption barrier for CH_3* species decreased from 70.0 to 50.6 kJ·mol^{-1}. Moreover, this desorption barrier was substantially lower than the activation barrier for the consecutive reaction between CH_3* and surface oxygen species. This finding suggests that elevated temperatures, induced by the LSPR effect of Au, facilitated CH_3* desorption, thereby increasing the likelihood of CH_3· recombination to form C_2H_6. Consequently, thermal input played a crucial role in enhancing both yield and selectivity in photocatalytic OCM reactions.

Unlike OCM, NOCM avoids the use of oxygen, achieving 100% atomic efficiency with H_2 as the sole byproduct[3, 94]. In addition to the kinetic requirements for the key steps such as C–C coupling and product desorption, elevated temperatures also help overcome

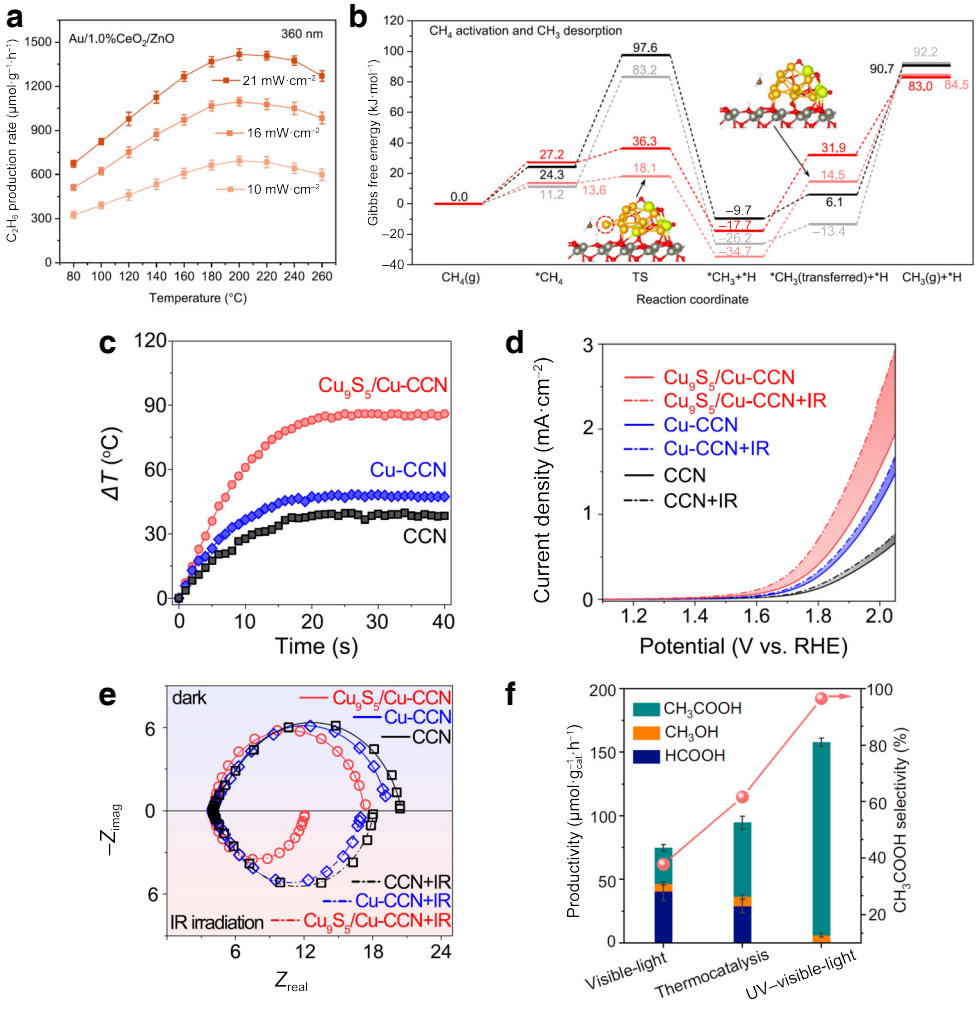

Fig. 4. Mechanisms behind thermo-assisted photocatalytic methane conversion to C_2 products. a, Investigation of thermal contributions on the Au/CeO_2/ZnO catalyst by varying temperature and irradiance. **b,** Evaluation of CH_4 activation and CH_3 desorption barriers on Au/ZnO (black) and Au/CeO_2/ZnO (red) at 25 °C (light colour) and 150 °C (dark colour). Reproduced with permission from Ref.[44], © Song, H. et al. 2025. **c,** Temperature responses under full-spectrum light irradiation over Cu_9S_5/Cu-CCN, Cu-CCN and CCN catalysts. **d,** Polarization curves and **e,** EIS Nyquist plots of CH_4 electrooxidation over Cu_9S_5/Cu-CCN, Cu-CCN and CCN catalysts with or without IR irradiation. Reproduced with permission from Ref.[99], © Xue, F. et al. 2024. **f,** CH_3COOH productivity and selectivity over RhZn-MoS_2/TiO_2 catalyst under various reaction conditions. Reproduced with permission from Ref.[100], © Li, Y. et al. 2025.

the thermodynamic limitations of NOCM[39]. As a result, many catalysts such as Nb-modified TiO_2-SiO_2[95], Ga-doped TiO_2-SiO_2[96], Pd/Ga_2O_3[91], and Nb_2O_5[97] have enabled NOCM processes via thermo-assisted photocatalysis. However, the role of thermal energy in these systems is often underexplored, with more emphasis placed on C–H bond polarisation or preactivation via surface engineering. Interestingly, a unique function of thermal energy in modulating surface frustrated Lewis pair (FLP) sites for photocatalytic methane activation has been discovered in the Ag/InO_xH_y catalyst[98]. In this system, thermal energy enhanced the *in-situ* generation of oxygen vacancies, forming In-V_o-In-OH FLP sites that polarised CH_4 and promoted heterolytic C–H cleavage into CH_3^- and H^+. Subsequently, photoholes oxidised CH_3^- to CH_3·, which underwent coupling to form ethane, while photoelectrons reduced H^+ to H·, which dimerised to H_2. This thermo-assisted photocatalytic process achieved an ethane production rate approximately 6.5 times higher than that of the photon-driven system alone. In contrast, the thermal driven system alone remained negligible due to insufficient temperature to overcome the C–H activation barrier. These findings broaden the role of thermal energy assistance, highlighting its capacity to dynamically generate surface-active sites and thereby enhance overall photocatalytic performance.

3.2.2 Ethanol

The direct conversion of methane to ethanol (CH_3CH_2OH) can be conceptually viewed as a hybrid of methane to methanol and methane to ethane pathways. Apart from the collision of CH_3· with oxygen-containing species (as discussed in Section 3.1.1), CH_3CH_2OH formation requires an additional C–C bond coupling step to extend the carbon chain beyond CH_3OH. Critically, this process demands precise activation to obtain both oxygen-containing radicals and methane-derived species, either -CH_3 or -CH_2, making photocatalysis more suitable than thermocatalysis as the dominant driving force. Many photocatalysts have been reported to be active for CH_4 conversion to CH_3CH_2OH[101–104], with polymeric bases frequently employed due to their ability to stabilise carbon-containing intermediates for chain growth rather than premature desorption[1, 101]. Given the complexity of the reaction, such as intermediate migration, transformation, diffusion, and desorption, thermal assistance is expected to further accelerate key kinetic steps to improve the yield and selectivity. As a result, thermo-assisted photocatalysis has emerged as a prevalent mechanism for ethanol synthesis, with conjugated polymers continuing to serve as the primary photocatalytic components[1, 99, 105, 106].

A notable example involves the integration of Cu_9S_5 nanoparticles onto crystalline carbon nitride[99]. The Cu_9S_5 exhibited broadband absorption (200–1350 nm), enabling efficient photo-to-thermo conversion and generating localised thermal fields up to ~ 90 °C under light irradiation (Fig. 4c). This *in-situ* thermal effect enhanced charge carrier transport and reduced overpotential (Figs. 4d and 4e), significantly improving CH_4 oxidation activity, as evidenced by lower activation energies compared to systems lacking Cu_9S_5. Furthermore, elevated local temperatures reduce the desorption energy of ethanol, enabling timely product release and preventing overoxidation. This strategy achieved a state-of-the-art ethanol selectivity of 94.8%.

3.2.3 Acetic acid

Compared to ethanol, the direct conversion of methane to acetic acid (CH_3COOH) remains sparsely explored. If both carbon atoms are directly from CH_4, the reaction requires precise control over differential oxidation states within a single catalytic system, one CH_4 molecule must be converted to a CH_3·, while another must be oxidised to a carbonyl species (e.g., CO* and CHO*). This complexity, combined with the involvement of reactive oxygen-containing radicals and the tendency of CHO/CO intermediates to overoxidise to CO_2[107, 108], significantly suppresses CH_3COOH yield.

To address this challenge, some studies have introduced CO as a co-fed second carbon source alongside CH_4[100]. A representative example of thermo-assisted photocatalytic methane conversion to acetic acid was achieved using a specially designed RhZn-MoS_2/TiO_2 catalyst. In this system, CH_4 was activated at the Zn-Mo bridge site to form CH_3 species, while CO adsorbed on adjacent Rh sites, enabling C–C coupling to form key intermediate CH_3CO species. This intermediate subsequently reacts with OH to yield CH_3COOH. High-energy UV photons served as the primary driving force, as evidenced by Fig. 4f. Under UV–visible-light irradiation, the CH_3COOH production rate was approximately 5.3 times higher than under visible light alone, and 2.6 times higher than under thermocatalytic conditions at the same reaction temperature (65 °C). While the reaction appeared to be feasible under either photocatalytic or thermocatalytic conditions alone, the synergistic effect of dual-energy input has not yet been thoroughly investigated or quantified.

Table 2 summarises representative advances in photo-thermo synergistic methane conversion to C_2 chemicals. Notably, all reported systems employed a thermo-assisted photocatalytic mode, which combined high-energy photons (typically UV–visible light) to activate the inert C–H bond with mild thermal energy (generally < 200 °C) to facilitate coupling among reactive intermediates. Flow reactors dominated gas-solid phase reactions due to their superior capability for enhancing mass transfer and enabling timely product removal. Consequently, C_2H_4/C_2H_6 production rates in flow reactors were often significantly higher, sometimes by more than two orders of magnitude, compared to batch reactors, even under much lower irradiance conditions or reaction temperatures. Interestingly, achieving high C_2H_4/C_2H_6 yield and selectivity appeared to require Au as an indispensable co-catalyst. This was not only attributed to its LSPR effect, which generated *in-situ* thermal fields, but more importantly to its unique ability to promote coupling[29]. As a result, Au/metal oxide composites (e.g., TiO_2, ZnO, and CeO_2) were the most widely adopted catalyst systems with only limited variation among oxide supports.

In contrast, for methane conversion to C_2 oxygenates (e.g., ethanol and acetic acid), batch reactors were generally preferred at this early stage. These systems typically involved gas-liquid-solid three-phase configurations, requiring more complex reactor designs, where liquid-phase stirring compensated for the inherently low mass transfer in gas-solid batch systems. However, the production rates of C_2 oxygenates remained modest, up to two orders of magnitude lower than those of C_2 hydrocarbons, and selectivity was often lower than 90%. These observations underscored the significant challenge of achieving controlled oxidation beyond bond formation. Unlike hydrocarbon-oriented systems that relied on metal oxides and Au, oxygenate-oriented systems broadened the catalyst scope to carbon-based materials such as covalent triazine frameworks (CTFs), graphitic carbon nitride (g-C_3N_4), and reduced graphene oxide (r-GO). These materials offered advantages in stabilising carbon-containing intermediates for chain growth. However, their more negative valence band positions compared to O 2p-based metal oxides might hinder C–H activation from a kinetic perspective.

Table 2 Representative examples of photo-thermo conversion of methane to C_2 chemicals

Catalyst	Photo-thermo synergistic type	Reaction conditions	Production rate ($\mu mol \cdot h^{-1}$)	C_2 selectivity (%)	Ref.
$Au/CeO_2/ZnO$	Thermo-assisted photocatalysis	Flow reactor, 20 mg catalyst, 300–800 nm light, 670 $mW \cdot cm^{-2}$, 162 °C	C_2H_6/C_2H_4: 319.18	80	[44]
Ag/InO_xH_y	Thermo-assisted photocatalysis	Flow reactor, 30 mg catalyst, 250–1050 nm light, 126.8 $mW \cdot cm^{-2}$, 200 °C	C_2H_6: 10.176	100	[98]
Zn-doped MgO/Al_2O_3	Thermo-assisted photocatalysis	Batch reactor, 10 mg catalyst, full spectrum, 9160 $mW \cdot cm^{-2}$, 325 °C	C_2H_6: 0.96	94.93	[109]
Au/Nb_2O_5	Thermo-assisted photocatalysis	Flow reactor, 5 mg catalyst, 320–780 nm light, 300 $mW \cdot cm^{-2}$, 86.1 °C	C_2H_6: 7.7	96	[110]
Au/CeO_2	Thermo-assisted photocatalysis	Flow reactor, 50 mg catalyst, 365 nm LED, 200 $mW \cdot cm^{-2}$, 150 °C	C_2H_6/C_2H_4: 757.5	93	[29]
Au/MgO	Thermo-assisted photocatalysis	Flow reactor, 5 mg catalyst, full spectrum, 290 °C	C_2H_6: 63.667	90.4	[90]
Au/TiO_2	Thermo-assisted photocatalysis	Flow reactor, 20 mg catalyst, 365 nm LED, 120 °C	C_2H_6/C_2H_4: 479	86	[30]
Nb_2O_5	Thermo-assisted photocatalysis	Batch reactor, 5 mg catalyst, 200–2500 nm light, 2000 $mW \cdot cm^{-2}$, 67 °C	C_2H_6: 3.004	88.3	[97]
Ni-doped MgO/Al_2O_3	Thermo-assisted photocatalysis	Flow reactor, 5 mg catalyst, 400–800nm, 1040 $mW \cdot cm^{-2}$, 150 °C	C_2H_6: 2.2715	97.8	[111]
Ga-doped TiO_2-SiO_2	Thermo-assisted photocatalysis	Batch reactor, 2 mg catalyst, 2200 $mW \cdot cm^{-2}$, 120 °C	C_2H_6: 1.04	82	[96]
$Au\text{-}ZnO/TiO_2$	Thermo-assisted photocatalysis	Flow reactor, 20 mg catalyst, 300–500 nm light, 500 $mW \cdot cm^{-2}$, 140 °C	C_2H_6/C_2H_4: 100.8	91	[88]
Nb-modified TiO_2-SiO_2	Thermo-assisted photocatalysis	Batch reactor, 100 mg catalyst, 100 °C	C_2H_6: 0.169	96.2	[95]
Pd/Ga_2O_3	Thermo-assisted photocatalysis	Flow reactor, 800 mg catalyst, 220–300 nm light, 20 $mW \cdot cm^{-2}$, 47 °C	C_2H_6: 0.51	/	[91]
PtO_x/CTF-1	Thermo-assisted photocatalysis	Flow reactor, 1000 mg catalyst, 365 nm LED, 100 $mW \cdot cm^{-2}$, 65 °C	C_2H_5OH: 167.6	79.6	[1]
Cu_9S_5/Cu-CCN	Thermo-assisted photocatalysis	Batch reactor, 10 mg catalyst, full spectrum, 400 $mW \cdot cm^{-2}$, 50 °C	C_2H_5OH: 5.497	94.8	[99]
$Ru/Zn\text{-}g\text{-}C_3N_4$	Thermo-assisted photocatalysis	Batch reactor, 100 mg catalyst, UV–vis light, 80 °C	C_2H_5OH: 50.045	72.5	[105]
RGO/TiO_2	Thermo-assisted photocatalysis	Batch reactor, 10 mg catalyst, simulated solar light, 100 $mW \cdot cm^{-2}$, 60 °C	C_2H_5OH: 0.3521	53	[106]
$RhZn\text{-}MoS_2/TiO_2$	Thermo-assisted photocatalysis	Batch reactor, 25 mg catalyst, 200–800 nm light, 1500 $mW \cdot cm^{-2}$, 65 °C	CH_3COOH: 3.8	96.5	[100]

Overall, despite the promising selectivity and productivity achieved in photo-thermo catalytic methane conversion to C_2 products, CH_4 conversion again remains a critical bottleneck. For instance, the very recent result PtO_x/CTF-1 with the highest ethanol production rate achieved only 2.3% CH_4 conversion[1]. Looking forward, flexible application of dual-energy catalytic modes is expected to unlock new reaction pathways. Insights may be drawn from methane conversion to C_1 oxygenates (Section 3.1), where photo-thermo cascade catalysis could be developed to accommodate multi-intermediate assembly while mitigating overoxidation.

3.3 Methane to syngas

The direct conversion of methane into syngas (H_2 and CO) primarily proceeds via two conventional pathways: SRM and DRM. In thermocatalytic processes, extremely high temperatures (typically 700–1000 °C) are required to achieve complete dehydrogenation of CH_4 and to reach favourable equilibrium conversions to syngas[24, 54, 112]. The integration of photons into these reactions is anticipated to contribute to three key aspects: 1) facilitating C–H bond activation at lower temperatures, thereby reducing energy consumption; 2) enabling the breaking of thermodynamic equilibrium; 3) enhancing catalyst stability against coke accumulation under reaction conditions. Among the four modes of photo-thermo synergistic catalysis, photon-enhanced thermocatalysis is particularly prominent, as discussed in Section 2.2. This is largely because this reaction does not necessitate precise or moderate C–H bond activation, making it well-suited for operation at elevated temperatures to fully accelerate reaction kinetics. Furthermore, the band structures of many photocatalysts are insufficient to simultaneously meet the redox potentials required for CH_4 and CO_2 activation in DRM.

Given the industrial maturity and commercial viability of thermocatalytic SRM[113], research attention to this reaction has been relatively limited. However, recent studies have shown that the introduction of photons can significantly enhance catalytic performance at a fixed reaction temperature. In other words, achieving the same syngas yield via a purely thermocatalytic process typically requires an increase in temperature by several tens of degrees Celsius[23, 24]. A representative example involves the construction of a Schottky junction between metallic nanoparticles and a semiconductor, such as Rh/TiO_2[24] (**Fig. 5a**). Upon interband

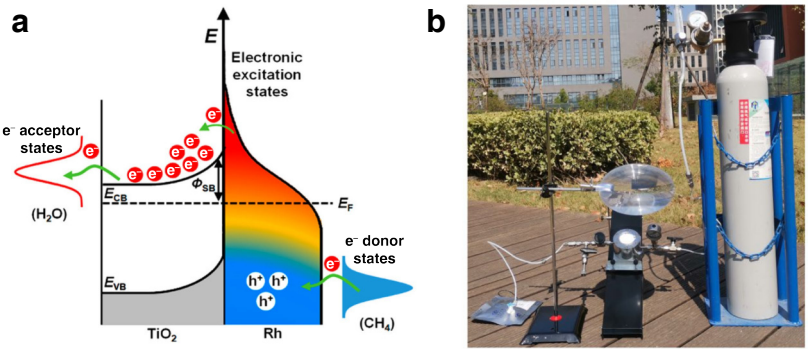

Fig. 5. Photo-enhanced thermocatalytic methane conversion to syngas. a, Substrate activation via excitation of hot carriers. Reproduced with permission from Ref.[24], © American Chemical Society 2018. **b,** Outdoor solar-driven DRM reaction setup. Reproduced with permission from Ref.[58], © American Chemical Society 2024.

photoexcitation, hot electrons generated in Rh nanoparticles can overcome the Schottky barrier and transfer to the TiO_2 conduction band, thereby prolonging their lifetime. This process left behind hot holes on the Rh surface, which facilitated the formation of $Rh^{\delta+}$ species. These positively charged Rh sites were highly effective in accelerating the rate-determining step (C–H bond activation in CH_4), leading to a substantial reduction, nearly 50%, in the activation energy compared to the thermocatalytic reaction under dark conditions. Consequently, a temperature increase of up to 40 °C was required in the absence of light to match the performance of the photo-enhanced thermocatalytic system.

Compared with SRM, DRM is often cited as an attractive route toward carbon neutrality as it co-consumes another dominant greenhouse gas of CO_2[114, 115]. However, it is more challenging than SRM due to the higher kinetic barrier associated with the higher bonding energy of C=O bond (~ 750 kJ·mol^{-1}) in CO_2 than O–H bond (~ 492 kJ·mol^{-1}) in H_2O[68], and the thermodynamic driving force for carbon deposition[54]. The research on photo-enhanced thermocatalysis is thus booming with a variety of catalysts (**Table 3**), mainly assembled of the form as metallic nanoparticles on metal oxide supports.

Due to the simultaneous generation of both localised thermal fields and hot carriers, the incorporation of metallic nanoparticles exhibiting LSPR effect has become a widely adopted strategy in photo-thermo catalysis[56, 116, 117]. For instance, plasmonic Cu nanoparticles could act as an antenna, while single Ru atoms served as active reaction sites[56]. This configuration enabled the development of an anti-coking and efficient catalyst that integrated both photo-enhanced thermocatalytic and photo-to-thermo conversion modes for DRM. The reaction was initiated with the dissociation of CH_4 and CO_2, forming surface-bound C*, O*, and H* species following CO release. In conventional thermocatalysis, H* species competed with C* for O*, often resulting in an imbalance between C* formation and removal, which led to coke accumulation. In contrast, hot carriers generated under light irradiation could significantly accelerate the associative desorption of H_2, thereby promoting the removal of H* and suppressing its reaction with O*. This facilitated the timely oxidation of C* species, effectively mitigating coke formation. Additionally, hot carriers enhanced the kinetics of CH_4 dehydrogenation, further improving catalytic efficiency. Under white-light illumination at an intensity of 19.2 W·cm^{-2}, the CuRu catalyst surface could reach temperatures of approximately 727 °C via photo-to-thermo conversion. At this temperature, the reaction rate was four times higher than that of the thermocatalytic process conducted at the same temperature. More importantly, the photo-thermo synergistic system exhibited excellent stability, with no noticeable deactivation observed over a 50-h test period, unlike the rapid deactivation (within 8 h) seen in the purely thermocatalytic counterpart.

In addition to the hot carriers generated in plasmonic metals, the photoelectrons/photoholes in traditional semiconductors have also shown the ability to accelerate the DRM reaction. Notably, some semiconductor-based systems have even exhibited the capacity to overcome the equilibrium limitations inherent to thermocatalytic DRM, as observed with catalysts such as $Rh/SrTiO_3$[25], Ni/CeO_2[57], and $CoNiRuRhPd/SrTiO_3$[58]. Taking the $Rh/SrTiO_3$ catalyst as an example, light served dual functions: inducing carrier excitation and maintaining reaction temperature through photo-to-thermo conversion. In this system, O^{2-} species served as intermediates for CO_2 reduction and CH_4 oxidation. When light was used as the sole driving force, photoelectrons from $SrTiO_3$ were transferred to Rh nanoparticles, where they reduced CO_2 to CO and generated O^{2-}. Subsequently, CH_4 was activated by these O^{2-} species in conjunction with photoholes, leading to H_2 production. This photon excitation has enabled the reaction to surpass the thermodynamic equilibrium limitations over a broad temperature range (120–500 nm due to interband transition, allowing the catalyst to harness the entire solar spectrum, integrating both photo-to-thermo and photo-enhanced modes[58]. As a result, this catalyst has demonstrated robust activity under outdoor conditions (Fig. 5b), achieving performance comparable to that under artificial light sources. This approach opens new opportunities for utilising abundant and clean solar energy to drive the DRM reaction with higher efficiency than conventional thermocatalytic processes, a trend that is increasingly evident in the field of photo-thermo catalytic DRM. Furthermore, the development of larger-scale outdoor reactors, such as the recently reported meter-scale system for CO_2 photo-thermo methanation[118], is highly anticipated to facilitate the practical application of these sustainable technologies.

3.4 Methane to C_3 chemicals

To date, few successful examples have achieved the selective conversion of methane to C_3 chemicals via photo-thermo synergistic catalysis[128, 129]. Remarkably, propane (C_3H_8), a valuable C_3 hydrocarbon, was produced using a widely studied catalyst, Au/TiO_2[128]. Unlocking a previously underappreciated function of thermal energy in thermo-assisted photocatalysis made great contributions to this unexpected outcome. Unlike the conventional role of thermal energy in accelerating surface reaction kinetics, this system revealed a new function: inducing surface active site

Table 3 Representative examples of photo-thermo synergistic catalytic DRM

Catalyst	Photo-thermo synergistic type	Reaction conditions	Production rate ($mmol \cdot h^{-1}$)	H_2/CO ratio	Ref.
Pt/black TiO_2	Photo-enhanced thermocatalysis	15 mg catalyst, visible light, 0.1 $W \cdot cm^{-2}$, 600 °C (external heating)	H_2: 1.425, CO: 4.05	0.35	[119]
Pt/TaN	Photo-enhanced thermocatalysis	100 mg catalyst, visible light, 0.42 $W \cdot cm^{-2}$, 500 °C (external heating)	H_2: 6.75, CO: 7.5	0.9	[120]
Ni/SiO_2	Photo-enhanced thermocatalysis	catalyst containing 30 mg metallic Ni, 300–800 nm, 1.07 $W \cdot cm^{-2}$, 550 °C (external heating)	H_2: 2.25, CO: 2.52	0.89	[121]
Rh-Au/SBA-15	Photo-enhanced thermocatalysis	5 mg catalyst, visible light, 0.32 $W \cdot cm^{-2}$, 500 °C (external heating)	H_2: 122.4, CO: 117	1.05	[117]
Pt-Au/SiO_2	Photo-enhanced thermocatalysis	20 mg catalyst, 300–800 nm, 0.6 $W \cdot cm^{-2}$, 400 °C (external heating)	H_2: 0.11, CO: 0.146	0.75	[116]
MgO/Pt/Zn-CeO_2	Photo-enhanced thermocatalysis + Photo-to-thermo catalysis	5 mg catalyst, solar simulator, 3 $W \cdot cm^{-2}$, 600 °C (external heating)	H_2: 1.78, CO: 2.58	0.69	[122]
Pt-Si-CeO_2	Photo-enhanced thermocatalysis + Photo-to-thermo catalysis	10 mg catalyst, solar simulator, 250–800 nm, 1.775 $W \cdot cm^{-2}$, 600 °C (external heating)	H_2: 0.9, CO: 1.54	0.58	[123]
Ni/Ga_2O_3	Photo-enhanced thermocatalysis + Photo-to-thermo catalysis	40 mg catalyst, UV–vis light, 3 $W \cdot cm^{-2}$, 391 °C (external heating)	H_2: 0.48, CO: 0.51	0.94	[124]
Ru/LaMnFeO	Photo-enhanced thermocatalysis + Photo-to-thermo catalysis	50 mg catalyst, 5.2 $W \cdot cm^{-2}$, 500 °C	H_2: 25.734, CO: 32.952	0.78	[26]
CoNiRuRhPd/$SrTiO_3$	Photo-enhanced thermocatalysis + Photo-to-thermo catalysis	5 mg catalyst, 200–2500 nm, 4 $W \cdot cm^{-2}$, 560 °C	H_2: 1.819, CO: 1.866	0.97	[58]
CuRu/MgO-Al_2O_3	Photo-enhanced thermocatalysis + Photo-to-thermo catalysis	1.5 mg catalyst, white light, 19.2 $W \cdot cm^{-2}$, 727 °C	H_2: 2.97, CO: 2.97	1	[56]
Ni/CeO_2	Photo-enhanced thermocatalysis + Photo-to-thermo catalysis	25 mg catalyst, 320–800 nm, 2.4 $W \cdot cm^{-2}$, 472 °C	H_2: 1.664, CO: 1.493	1.11	[57]
Ru/MgO	Photo-enhanced thermocatalysis + Photo-to-thermo catalysis	10 mg catalyst, UV–vis–IR light, 7.32 $W \cdot cm^{-2}$, 490 °C	H_2: 26.106, CO: 35.586	0.73	[125]
RuNi single-atom alloy	Photo-enhanced thermocatalysis + Photo-to-thermo catalysis	5 mg catalyst, full spectrum, 13.5 $W \cdot cm^{-2}$, 350 °C	H_2: 2.694, CO: 3.21	0.84	[126]
Rh/$LaNiO_3$	Photo-enhanced thermocatalysis + Photo-to-thermo catalysis	100 mg catalyst, 300–1100nm, 1.5 $W \cdot cm^{-2}$	H_2: 0.452, CO: 0.528	0.86	[127]
Rh/$SrTiO_3$	Photo-enhanced thermocatalysis + Photo-to-thermo catalysis	5 mg catalyst, 450 °C	H_2: 0.372, CO: 0.372	~ 1	[25]

reconstruction. At a surface temperature of approximately 200 °C, co-fed steam induced tensile strain on Au nanoparticles, significantly enhancing their interaction with both CH_4 reactants and C_2H_6 intermediates. This promoted C–H activation and facilitated C_2–C_1 coupling to form propane. In parallel, steam played a second critical role by thermally activating lattice oxygen to generate active hydroxyl species near the Au/TiO_2 interface. These hydroxyls promoted the combustion of surface-bound hydrogen species formed during C–H activation, thereby regenerating the Au surface and accelerating the overall catalytic cycle. As a result of this dual thermal function, the C_3H_8 yield driven by UV-photons increased nearly sixfold compared to room temperature conditions, with selectivity improving from 50.8% to 90%. This work compellingly demonstrates how the strategic use of photo-thermo synergy can unlock new reaction pathways and achieve breakthroughs in methane valorisation products.

4 Challenges and perspectives

Significant progress has been made in the development of photo-thermo synergistic catalytic systems for methane conversion. This dual-energy-driven approach has demonstrated clear advantages: enhanced reactivity compared to conventional photocatalysis (e.g., POM and OCM), and improved selectivity and/or reduced energy consumption relative to conventional thermocatalysis (e.g., SRM and DRM). In some cases, stable methane conversion has even been achieved using natural outdoor solar energy, underscoring the potential for sustainable operation. Despite these promising developments, the field still faces at least five challenges that must be addressed to enable broader application and scalability.

4.1 Scientific evaluation of performance

The enhanced performance of photo-thermo synergistic catalysis can be evaluated across multiple dimensions, depending on the reaction type, ranging from chemical metrics such as conversion and selectivity to photophysical parameters like quantum efficiency and solar-to-chemical conversion efficiency. Among these, temperature emerges as a critical factor influencing nearly all performance indicators. Accurate temperature measurement is therefore essential for enabling objective and scientifically robust comparisons across different catalyst materials and systems. This becomes particularly important when making ambitious claims, such as the frequently cited "breaking of thermodynamic equilibrium limitation in DRM"[25, 58]. It should be noted that even slight temperature increases can lead to exponential rises in conversion, especially when operating near the inflection point of the "light-off" curve in thermocatalysis[43, 130].

Given that photon penetration depth is typically on the micrometre scale[131, 132], functional photo-to-thermo components

are often confined to ultrathin layers. Conventional thermocouples, with probe diameters on the millimetre scale, can introduce significant discrepancies between actual surface temperatures and measured values[133]. Even infrared (IR) cameras, commonly used to monitor thermal distribution, may yield misleading results due to variations in material reflectance and blackbody radiation properties[53]. These inaccuracies are particularly pronounced in nanoscale systems with efficient photo-to-thermo conversion, such as those involving plasmonic metallic nanoparticles. In such cases, underestimating the true temperature may lead to misclassification of the catalytic mechanism, for example, mistaking photo-to-thermo catalysis for photo-enhanced thermocatalysis, thereby exaggerating the role of photons.

To address these challenges, the development and implementation of advanced temperature measurement techniques, such as operando X-ray absorption nanothermometry[134] and operando luminescence thermometry[135], are strongly recommended. These methods offer high spatial resolution and can provide more accurate insights into the thermal microenvironments of the catalytic systems. Additionally, when investigating the specific promotional role of photons, it is advisable to use low-intensity light sources during control experiments to minimise photo-to-thermo effects, as shown in the $Au/CeO_2/ZnO$ system discussed in Section 3.2.1. Furthermore, using light sources of different wavelengths to achieve the same surface temperature can help identify the contribution of photons. If a higher activity can only be observed under light with sufficient energy to excite energetic carriers, this supports the presence of a photocatalytic process. Wherever possible, accurate surface temperature data should be reported when comparing catalytic performance metrics. Ideally, experiments should be conducted under consistent temperature conditions to ensure fair and meaningful comparisons across different systems.

4.2 Expanding the scope of valuable products

To date, photo-thermo synergistic catalysis has primarily focused on methane conversion to C_1–C_2 products. While this includes important compounds such as methanol and formaldehyde, the overall product spectrum remains narrow. For example, in OCM and NOCM processes, C_2H_6 is typically the dominant C_2 product, whereas C_2H_4, a highly valuable industrial feedstock, is far less explored. Similarly, although higher hydrocarbons (C_n, $n > 2$) have been reported in OCM or NOCM processes, their selectivity is generally low, with only one notable example achieving 91.3% selectivity to propane (C_3H_8). In contrast, desired products such as ethylene[136, 137] and benzene[4, 138] have already been successfully achieved using either photocatalysis or thermocatalysis alone. Many existing pathways are based on either thermo-assisted photocatalysis or photo-enhanced thermocatalysis, where one energy mode dominates, resulting in product types that largely follow single-energy-driven pathways. The potential flexibility and diversity offered by treating photocatalysis and thermocatalysis as equally influential processes remain underutilised, yet this approach holds promise for expanding the product scope.

Achieving this goal requires a comprehensive understanding of reaction pathways, including the behaviour of all substrates and intermediates, and their possible transformation routes under different energy inputs. Photo-thermo cascade catalysis offers a compelling example, where temporal and spatial separation of functional components enables cooperative synthesis, as shown in the production of HCHO and HCOOH (see Section 3.1.2 and Section 3.1.3). This concept could be extended to multi-step transformations, for instance, using photoactivation to generate ethane, followed by thermocatalytic or photo-thermo catalytic dehydrogenation to produce ethylene. A similar strategy has been shown in CO_2 photocatalytic hydrogenation to C_2H_4[139], where CO_2 was first reduced to C_2H_6 by Au/TiO_2, and then dehydrogenated to C_2H_4 by PdZn-ZnO, showcasing the potential of cascade reactions. Beyond tandem reactions, it is also highly promising to simultaneously apply photo and thermo energy to activate different components or substrates, allowing products to emerge from the recombination of intermediates formed via photocatalysis and thermocatalysis, respectively. Through these strategies, new catalytic systems capable of orchestrating complex transformations toward higher-value products with high selectivity may soon become a reality, breaking the product limitations imposed by single-energy-driven approaches.

4.3 Development of dual-energy *in-situ* characterisations

To obtain a comprehensive understanding of the photo-thermo catalytic methane conversion, it is essential to unravel both the photophysics and surface chemistry under real reaction conditions. *In-situ*/operando characterisation techniques are therefore indispensable. However, their development and application have lagged behind, as most current *in-situ*/*operando* studies rely on single-energy input paradigms, investigating either photocatalysis or thermocatalysis in isolation. For instance, *in-situ* ATR-FTIR or DRIFTS measurements under light irradiation without thermal input are commonly used to probe surface chemistry during photo-thermo catalytic processes[29, 30, 58]. While these approaches provide partial mechanistic insights, they may overlook intermediates or active species that require co-driven activation by both photon and thermal energy. This challenge is even greater in understanding photophysics. Apart from being conducted under ideal inert conditions, almost no studies have thoroughly resolved charge dynamics and energy conversion among photons, phonons, electrons, and holes under photo-thermo catalytic conditions. Yet, carrier behaviour can differ significantly under thermal heating[31, 140, 141], such as enhanced collision-induced decay due to lattice vibrations and phonon-assisted release of carriers trapped in shallow states. Consequently, no mature mechanistic framework currently exists to guide material design for balancing interactions among multiple functional components.

To address these gaps, the development of dual-energy *in-situ* characterisation techniques tailored to new catalytic modes is urgently needed, enabling the elucidation of synergistic interactions between photocatalytic components and thermocatalytic components at the atomic scale[142]. For *in-situ* techniques widely used in thermocatalysis, such as DRIFTS and XPS, upgrades can be relatively straightforward by replacing window materials to allow light penetration. However, for more complex systems, such as synchrotron X-ray absorption spectroscopy, designing dedicated cells requires a deep understanding of measurement and instrumental constraints. For techniques where significant improvements are challenging in the short term, alternative strategies should be considered to approximate dual-energy conditions. For example, in photophysic studies where introducing a heating element is impractical, low-energy light sources (e.g., IR) could be employed to induce thermal effects via photo-to-thermo conversion without interfering with primary excitation. In the long

term, the development of advanced dual-energy *in-situ* characterization platforms with precise control over both photon and thermal inputs remains strongly encouraged. Such tools will be critical for elucidating fundamental mechanisms and guiding the rational design of next-generation photo-thermo catalytic systems.

4.4 Reactor design optimisation

Compared to the rapid progress in catalyst development and the emergence of various synergistic catalytic modes, the design of dedicated photo-thermo catalytic reactors remains underdeveloped. A key challenge arises from the fundamental difference between light and heat conduction: light typically propagates in two dimensions with limited surface penetration, whereas heat distributes three-dimensionally throughout bulk materials[33, 143]. Fixed-bed reactors, widely used in both photocatalysis and thermocatalysis, suffer significantly from these limitations when applied to photo-thermo synergistic catalysis. From the perspective of light conduction, catalyst bed thickness is critical, as photons typically penetrate only ~ 0.1 μm[131], leaving most of the deeper catalyst layers inactive. This issue becomes even more pronounced in photo-to-thermo catalysis, where steep temperature gradients can develop within the bed. Similarly, for systems employing external heating elements, thick fixed beds can lead to inhomogeneous temperature distribution. These factors may result in surface and bulk catalysts operating under entirely different mechanisms, such as photo-thermo catalysis combined with thermocatalysis or photocatalysis combined with thermocatalysis, posing significant challenges for performance optimisation and mechanistic interpretation.

Greater effort is needed to develop reactors tailored to specific photo-thermo reactions to achieve uniform light and heat conduction. Strategies include engineering porous structures to enhance light penetration and designing interchannels to facilitate efficient heat transfer. Reactor configurations may need to move beyond traditional fixed-bed designs toward innovative models, such as membrane reactors, foam reactors, and fluidised reactors[43, 144]. Additionally, advanced elements should be integrated to improve energy delivery and maximise catalyst exposure, such as optical fibre-guided illumination and parabolic solar concentrators[31, 38]. Beyond optimising light and heat conduction, reactor design should also accommodate the unique requirements of photo-thermo synergistic catalysis to improve overall performance. As shown in Section 3.1.3, in the methane to formic acid system using CsPW-TiO_2 and Ru/Al_2O_3, reactor engineering was leveraged to achieve spatial separation of reaction steps, an outcome difficult to accomplish through material design alone. Finally, given the abundance of solar energy as a source of both photocatalytic and thermocatalytic components via different photon energies, future research should focus on developing outdoor compatible reactor systems, such as arrayed panel reactors or tower-type solar concentrator reactors, to enable real-world application and scalability of photo-thermo catalytic methane conversion[145, 146].

4.5 Artificial intelligence (AI)-assisted catalyst discovery

Currently, research efforts in photo-thermo catalysis predominantly emphasise the photocatalytic component, even in photo-enhanced thermocatalysis, where studies focus on introducing functional elements capable of generating energetic carriers. Consequently, catalyst development largely relies on trial-and-error or semi-empirical strategies, typically combining oxide semiconductors (e.g., TiO_2 and ZnO) with co-catalysts (e.g., Au, Cu, Pt, and Ni) to assemble multiple functionalities such as plasmonic effects and Schottky junctions. Meanwhile, phonons generally act at the system level rather than being tailored to specific catalytic species, with thermal energy added as an auxiliary input (e.g., Au/TiO_2, Au/CeO_2, and Au/ZnO/TiO_2; see Section 3.2.1). This imbalance limits the scope of photo-thermo catalysts and constrains exploration of the full potential of dual-energy-driven catalytic modes for reactions beyond single-energy paradigms. As shown in Section 3.1.3, dedicated design of thermocatalytic components can deliver unexpected synergistic effects, achieving selectivity unattainable under single-energy conditions.

To unlock this potential, thermocatalytic components must be elevated to an equal position alongside photocatalytic components, enabling holistic consideration of reaction pathways across different photo-thermo synergistic modes. Beyond photophysical properties such as band structure, carrier density, interface junctions, and light absorption, thermochemical characteristics, including d-band centre, surface acidity and polarity, hybridisation configuration, porosity and thermal conductivity, should also be prioritised. Furthermore, the catalyst library should expand beyond oxide semiconductors to encompass diverse compositions, leveraging tunable polymers, high-surface-area frameworks (e.g., molecular sieves, silica, and MOFs), and multifunctional systems such as high-entropy alloys and heterojunctions. Given this complexity, artificial intelligence offers a powerful approach to accelerate catalyst discovery and optimisation[142, 147]. By constructing a comprehensive materials database that integrates existing photo-thermo systems and extend to photocatalytic and thermocatalytic platforms, AI models can identify hidden patterns, predict performance, and propose novel catalyst combinations. This data-driven approach holds significant promise to guide the rational design of next-generation photo-thermo synergistic catalysts for methane conversion.

References

[1] Xie, J. J.; Fu, C.; Quesne, M. G.; Guo, J.; Wang, C.; Xiong, L. Q.; Windle, C. D.; Gadipelli, S.; Guo, Z. X.; Huang, W. X. et al. Methane oxidation to ethanol by a molecular junction photocatalyst. *Nature* **2025**, *639*, 368–374.

[2] Xie, Z. H.; Huang, E. W.; Turaczy, K. K.; Garg, S.; Hwang, S.; Kasala, P. R.; Liu, P.; Chen, J. G. Biogas sequestration to carbon nanofibers via tandem catalytic strategies. *Nat. Chem. Eng.* **2025**, *2*, 118–129.

[3] Zhang, W. Q.; Fu, C. F.; Low, J.; Duan, D. L.; Ma, J.; Jiang, W. B.; Chen, Y. H.; Liu, H. J.; Qi, Z. M.; Long, R. et al. High-performance photocatalytic nonoxidative conversion of methane to ethane and hydrogen by heteroatoms-engineered TiO_2. *Nat. Commun.* **2022**, *13*, 2806.

[4] Guo, X. G.; Fang, G. Z.; Li, G.; Ma, H.; Fan, H. J.; Yu, L.; Ma, C.; Wu, X.; Deng, D. H.; Wei, M. M. et al. Direct, nonoxidative conversion of methane to ethylene, aromatics, and hydrogen. *Science* **2014**, *344*, 616–619.

[5] Liu, G.; Shen, L.; Ciais, P.; Lin, X.; Hauglustaine, D.; Lan, X.; Turner, A. J.; Xi, Y.; Zhu, Y.; Peng, S. S. Trends in the seasonal amplitude of atmospheric methane. *Nature* **2025**, *641*, 660–665.

[6] Li, X. Y.; Wang, C.; Tang, J. W. Methane transformation by photocatalysis. *Nat. Rev. Mater.* **2022**, *7*, 617–632.

[7] Mao, J.; Liu, H.; Cui, X. J.; Zhang, Y. L.; Meng, X. Y.; Zheng, Y. P.; Chen, M. S.; Pan, Y.; Zhao, Z. C.; Hou, G. J. et al. Direct conversion

of methane with O_2 at room temperature over edge-rich MoS_2. *Nat. Catal.* **2023**, *6*, 1052–1061.

[8] Zakaria, Z.; Kamarudin, S. K. Direct conversion technologies of methane to methanol: An overview. *Renew. Sustain. Energy Rev.* **2016**, *65*, 250–261.

[9] Zhu, Q. J.; Wegener, S. L.; Xie, C.; Uche, O.; Neurock, M.; Marks, T. J. Sulfur as a selective 'soft' oxidant for catalytic methane conversion probed by experiment and theory. *Nat. Chem.* **2013**, *5*, 104–109.

[10] Schwach, P.; Pan, X. L.; Bao, X. H. Direct conversion of methane to value-added chemicals over heterogeneous catalysts: Challenges and prospects. *Chem. Rev.* **2017**, *117*, 8497–8520.

[11] Song, H.; Huang, H. M.; Meng, X. G.; Wang, Q.; Hu, H. L.; Wang, S. Y.; Zhang, H. W.; Jewasuwan, W.; Fukata, N.; Feng, N. D. et al. Atomically dispersed nickel anchored on a nitrogen-doped carbon/TiO_2 composite for efficient and selective photocatalytic CH_4 oxidation to oxygenates. *Angew. Chem., Int. Ed.* **2023**, *62*, e202215057.

[12] Yuliati, L.; Yoshida, H. Photocatalytic conversion of methane. *Chem. Soc. Rev.* **2008**, *37*, 1592–1602.

[13] Li, Q.; Ouyang, Y. X.; Li, H. L.; Wang, L. B.; Zeng, J. Photocatalytic conversion of methane: Recent advancements and prospects. *Angew. Chem.* **2022**, *134*, e202108069.

[14] Xu, Y. X.; Chen, E. Q.; Tang, J. W. Photocatalytic methane conversion to high-value chemicals. *Carbon Future* **2024**, *1*, 9200004.

[15] Lee, C. W.; Kim, J. H.; Bootharaju, M. S.; Hyeon, T.; Lee, B. H. Synthesis of high-performance photocatalysts for solar-driven hydrogen production and carbon dioxide reduction. *Carbon Future* **2024**, *1*, 9200025.

[16] Matter, F.; Niederberger, M. The importance of the macroscopic geometry in gas-phase photocatalysis. *Adv. Sci.* **2022**, *9*, 2105363.

[17] Jin, H. G.; Zhao, P. C.; Qian, Y. Y.; Xiao, J. D.; Chao, Z. S.; Jiang, H. L. Metal-organic frameworks for organic transformations by photocatalysis and photothermal catalysis. *Chem. Soc. Rev.* **2024**, *53*, 9378–9418.

[18] Li, X. R.; Chen, Y.; Tao, Y.; Shen, L.; Xu, Z. M.; Bian, Z. F.; Li, H. X. Challenges of photocatalysis and their coping strategies. *Chem Catal.* **2022**, *2*, 1315–1345.

[19] Wu, X. J.; Zhang, H. Z.; Xie, S. J.; Wang, Y. Photocatalytic conversion of methane: Catalytically active sites and species. *Chem Catal.* **2023**, *3*, 100437.

[20] Xu, C.; Tang, Q. J.; Tu, W. G.; Wang, L. Photon and phonon powered photothermal catalysis. *Energy Environ. Sci.* **2024**, *17*, 4461–4480.

[21] Wang, H.; Harkou, E.; Constantinou, A.; Al-Salemc, S. M.; Manos, G.; Tang, J. W. From photocatalysis to photon-phonon co-driven catalysis for methanol reforming to hydrogen and valuable by-products. *Chem. Soc. Rev.* **2025**, *54*, 2188–2207.

[22] Mateo, D.; Cerrillo, J. L.; Durini, S.; Gascon, J. Fundamentals and applications of photo-thermal catalysis. *Chem. Soc. Rev.* **2021**, *50*, 2173–2210.

[23] Han, B.; Wei, W.; Li, M. J.; Sun, K.; Hu, Y. H. A thermo-photo hybrid process for steam reforming of methane: Highly efficient visible light photocatalysis. *Chem. Commun.* **2019**, *55*, 7816–7819.

[24] Song, H.; Meng, X. G.; Wang, Z. J.; Wang, Z.; Chen, H. L.; Weng, Y. X.; Ichihara, F.; Oshikiri, M.; Kako, T.; Ye, J. H. Visible-light-mediated methane activation for steam methane reforming under mild conditions: A case study of Rh/TiO_2 catalysts. *ACS Catal.* **2018**, *8*, 7556–7565.

[25] Shoji, S.; Peng, X. B.; Yamaguchi, A.; Watanabe, R.; Fukuhara, C.; Cho, Y.; Yamamoto, T.; Matsumura, S.; Yu, M. W.; Ishii, S. et al. Photocatalytic uphill conversion of natural gas beyond the limitation of thermal reaction systems. *Nat. Catal.* **2020**, *3*, 148–153.

[26] Li, J. L.; Zhao, J. W.; Wang, S. B.; Peng, K. S.; Su, B.; Liu, K. L.; Hung, S. F.; Huang, M. R.; Zhang, G. G.; Zhang, H. B. et al. Activating lattice oxygen in perovskite ferrite for efficient and stable photothermal dry reforming of methane. *J. Am. Chem. Soc.* **2025**, *147*, 14705–14714.

[27] Xu, Y. X.; Wang, C.; Li, X. Y.; Xiong, L. Q.; Zhang, T. Y.; Zhang, L. Q.; Zhang, Q. H.; Gu, L.; Lan, Y.; Tang, J. W. Efficient methane oxidation to formaldehyde via photon-phonon cascade catalysis. *Nat. Sustain.* **2024**, *7*, 1171–1181.

[28] Hao, Y. C.; Chen, L. W.; Liu, H. D.; Nie, W. F.; Ge, X. J.; Li, J. N.; Huang, H. Z.; Sun, C.; Lv, C. C.; Ning, S. B. et al. Continuous photo-oxidation of methane to methanol at an atomically tailored reticular gas-solid interface. *Nat. Commun.* **2025**, *16*, 747.

[29] Wang, C.; Xu, Y. X.; Xiong, L. Q.; Li, X. Y.; Chen, E. Q.; Miao, T. J.; Zhang, T. Y.; Lan, Y.; Tang, J. W. Selective oxidation of methane to C_{2+} products over Au–CeO_2 by photon-phonon co-driven catalysis. *Nat. Commun.* **2024**, *15*, 7535.

[30] Li, X. Y.; Li, C.; Xu, Y. X.; Liu, Q.; Bahri, M.; Zhang, L. Q.; Browning, N. D.; Cowan, A. J.; Tang, J. W. Efficient hole abstraction for highly selective oxidative coupling of methane by Au-sputtered TiO_2 photocatalysts. *Nat. Energy* **2023**, *8*, 1013–1022.

[31] Fang, S. Y.; Hu, Y. H. Thermo-photo catalysis: A whole greater than the sum of its parts. *Chem. Soc. Rev.* **2022**, *51*, 3609–3647.

[32] Zacharias, M.; Patrick, C. E.; Giustino, F. Stochastic approach to phonon-assisted optical absorption. *Phys. Rev. Lett.* **2015**, *115*, 177401.

[33] Ramos-Fernandez, E. V.; Rendon-Patiño, A.; Mateo, D.; Wang, X. H. L.; Dally, P.; Cui, M. M.; Castaño, P.; Gascon, J. Photothermal catalysts, light and heat management: From materials design to performance evaluation. *Adv. Energy Mater.* **2025**, *15*, 2405272.

[34] Lin, L. T.; Xing, D. N.; Zhang, C. Y.; Liu, Y. Y.; Wang, Z. Y.; Wang, P.; Zheng, Z. K.; Cheng, H. F.; Dai, Y.; Huang, B. B. Enhanced thermal assisted photocatalysis reduction of carbon dioxide over a $Fe_{2-x}Ga_xO_3$ solid solution. *Catal. Sci. Technol.* **2023**, *13*, 3638–3644.

[35] Gan, Z. X.; Wu, X. L.; Meng, M.; Zhu, X. B.; Yang, L.; Chu, P. K. Photothermal contribution to enhanced photocatalytic performance of graphene-based nanocomposites. *ACS Nano* **2014**, *8*, 9304–9310.

[36] Yang, M. Q.; Gao, M. M.; Hong, M. H.; Ho, G. W. Visible-to-NIR photon harvesting: Progressive engineering of catalysts for solar-powered environmental purification and fuel production. *Adv. Mater.* **2018**, *30*, 1802894.

[37] Song, C. Q.; Wang, Z. H.; Yin, Z.; Xiao, D. Q.; Ma, D. Principles and applications of photothermal catalysis. *Chem Catal.* **2022**, *2*, 52–83.

[38] Xie, B. Q.; Hu, D.; Kumar, P.; Ordomsky, V. V.; Khodakov, A. Y.; Amal, R. Heterogeneous catalysis via light-heat dual activation: A path to the breakthrough in C1 chemistry. *Joule* **2024**, *8*, 312–333.

[39] Song, H.; Meng, X. G.; Wang, Z. J.; Liu, H. M.; Ye, J. H. Solar-energy-mediated methane conversion. *Joule* **2019**, *3*, 1606–1636.

[40] Li, X. Y.; Wang, C.; Yang, J. L.; Xu, Y. X.; Yang, Y.; Yu, J. G.; Delgado, J. J.; Martsinovich, N.; Sun, X.; Zheng, X. S. et al. PdCu nanoalloy decorated photocatalysts for efficient and selective oxidative coupling of methane in flow reactors. *Nat. Commun.* **2023**, *14*, 6343.

[41] Jiang, Y. H.; Li, S. Y.; Wang, S. K.; Zhang, Y.; Long, C.; Xie, J.; Fan, X. Y.; Zhao, W. S.; Xu, P.; Fan, Y. Y. et al. Enabling specific photocatalytic methane oxidation by controlling free radical type. *J. Am. Chem. Soc.* **2023**, *145*, 2698–2707.

[42] Li, X. Y.; Xie, J. J.; Rao, H.; Wang, C.; Tang, J. W. Platinum- and CuO_x-decorated TiO_2 photocatalyst for oxidative coupling of

methane to C_2 hydrocarbons in a flow reactor. *Angew. Chem., Int. Ed.* **2020**, *59*, 19702–19707.

[43] Wang, R. Y.; Liu, D.; Li, Q.; Xuan, Y. M.; Jin, H. G.; Guo, L. J. Photothermal catalysis: A viewpoint from exergy. *Energy Environ. Sci.* **2025**, *18*, 9302–9311.

[44] Song, H.; Sun, K.; Huang, H. M.; Ning, S. B.; Wang, S. Y.; Wang, Z.; Weng, Y. X.; Cui, Y.; Li, Y. F.; Wang, X. S. et al. Integrating photochemical and photothermal effects for selective oxidative coupling of methane into C_{2+} hydrocarbons with multiple active sites. *Nat. Commun.* **2025**, *16*, 2831.

[45] Habisreutinger, S. N.; Schmidt-Mende, L.; Stolarczyk, J. K. Photocatalytic reduction of CO_2 on TiO_2 and other semiconductors. *Angew. Chem., Int. Ed.* **2013**, *52*, 7372–7408.

[46] Yu, X.; Zholobenko, V. L.; Moldovan, S.; Hu, D.; Wu, D.; Ordomsky, V. V.; Khodakov, A. Y. Stoichiometric methane conversion to ethane using photochemical looping at ambient temperature. *Nat. Energy* **2020**, *5*, 511–519.

[47] Li, X.; Yu, J. G.; Jaroniec, M. Hierarchical photocatalysts. *Chem. Soc. Rev.* **2016**, *45*, 2603–2636.

[48] Wang, Z. J.; Song, H.; Liu, H. M.; Ye, J. H. Coupling of solar energy and thermal energy for carbon dioxide reduction: Status and prospects. *Angew. Chem., Int. Ed.* **2020**, *59*, 8016–8035.

[49] Xie, B. Q.; Wong, R. J.; Tan, T. H.; Higham, M.; Gibson, E. K.; Decarolis, D.; Callison, J.; Aguey-Zinsou, K. F.; Bowker, M.; Catlow, C. R. A. et al. Synergistic ultraviolet and visible light photoactivation enables intensified low-temperature methanol synthesis over copper/zinc oxide/alumina. *Nat. Commun.* **2020**, *11*, 1615.

[50] Meng, L. S.; Chen, Z. Y.; Ma, Z. Y.; He, S.; Hou, H. H.; Yuan, R. S.; Huang, X. H.; Wang, X. X.; Wang, X. C. et al. Gold plasmon-induced photocatalytic dehydrogenative coupling of methane to ethane on polar oxide surfaces. *Energy Environ. Sci.* **2018**, *11*, 294–298.

[51] Feng, X. L.; Liu, D. P.; Yan, B. L.; Shao, M. Z.; Hao, Z. M.; Yuan, G. B.; Yu, H. H.; Zhang, Y. Highly active $PdO/Mn_3O_4/CeO_2$ nanocomposites supported on one dimensional halloysite nanotubes for photoassisted thermal catalytic methane combustion. *Angew. Chem., Int. Ed.* **2021**, *60*, 18552–18556.

[52] Wei, W. Q.; Wei, Z.; Li, R. Z.; Li, Z. H.; Shi, R.; Ouyang, S. X.; Qi, Y. H.; Philips, D. L.; Yuan, H. Subsurface oxygen defects electronically interacting with active sites on In_2O_3 for enhanced photothermocatalytic CO_2 reduction. *Nat. Commun.* **2022**, *13*, 3199.

[53] Jiang, H. Y.; Wang, L. Y.; Kaneko, H.; Gu, R. T.; Su, G. X.; Li, L.; Zhang, J.; Song, H. C.; Zhu, F.; Yamaguchi, A. et al. Light-driven CO_2 methanation over Au-grafted $Ce_{0.95}Ru_{0.05}O_2$ solid-solution catalysts with activities approaching the thermodynamic limit. *Nat. Catal.* **2023**, *6*, 519–530.

[54] Pakhare, D.; Spivey, J. A review of dry (CO_2) reforming of methane over noble metal catalysts. *Chem. Soc. Rev.* **2014**, *43*, 7813–7837.

[55] Xiong, H. L.; Dai, Z. H.; Fu, C. F.; Ji, X. M.; Dong, Y. Y.; Ge, M.; Long, R.; Bi, Y. P.; Xiong, Y. J. Constructing dynamic $Rh^{\delta+}$–O_v–Ti interfacial sites for highly efficient and stable photothermal catalytic methane dry reforming. *J. Am. Chem. Soc.* **2025**, *147*, 38204–38214.

[56] Zhou, L. N.; Martirez, J. M. P.; Finzel, J.; Zhang, C.; Swearer, D. F.; Tian, S.; Robatjazi, H.; Lou, M. H.; Dong, L. L.; Henderson, L. et al. Light-driven methane dry reforming with single atomic site antenna-reactor plasmonic photocatalysts. *Nat. Energy* **2020**, *5*, 61–70.

[57] Rao, Z. Q.; Wang, K. W.; Cao, Y. H.; Feng, Y. B.; Huang, Z. A.; Chen, Y. L.; Wei, S. Q.; Liu, L. Y.; Gong, Z. M.; Cui, Y. et al. Light-reinforced key intermediate for anticoking to boost highly durable methane dry reforming over single atom Ni active sites on CeO_2. *J. Am. Chem. Soc.* **2023**, *145*, 24625–24635.

[58] Xiong, H. L.; Dong, Y. Y.; Hu, C. Y.; Chen, Y. H.; Liu, H. J.; Long, R.; Kong, T. T.; Xiong, Y. J. Highly efficient and selective light-driven dry reforming of methane by a carbon exchange mechanism. *J. Am. Chem. Soc.* **2024**, *146*, 9465–9475.

[59] Guo, C.; Cui, Y.; Zhang, W. Q.; Du, X. Y.; Peng, X.; Yu, Y.; Li, J.; Wu, Y. L.; Huang, Y. C.; Kong, T. T. et al. Light-driven metal exsolution-redissolution of high-entropy oxide enabling high-performance dry reforming of methane. *Adv. Mater.* **2025**, *37*, 2500928.

[60] Hu, D.; Addad, A.; Ben Tayeb, K.; Ordomsky, V. V.; Khodakov, A. Y. Thermocatalysis enables photocatalytic oxidation of methane to formic acid at room temperature beyond the selectivity limits. *Cell Rep. Phys. Sci.* **2023**, *4*, 101277.

[61] Brongersma, M. L.; Halas, N. J.; Nordlander, P. Plasmon-induced hot carrier science and technology. *Nat. Nanotechnol.* **2015**, *10*, 25–34.

[62] Jiang, N. N.; Zhuo, X. L.; Wang, J. F. Active plasmonics: Principles, structures, and applications. *Chem. Rev.* **2018**, *118*, 3054–3099.

[63] Cui, X. M.; Ruan, Q. F.; Zhuo, X. L.; Xia, X. Y.; Hu, J. T.; Fu, R. F.; Li, Y.; Wang, J. F.; Xu, H. X. Photothermal nanomaterials: A powerful light-to-heat converter. *Chem. Rev.* **2023**, *123*, 6891–6952.

[64] Mao, C. L.; Li, H.; Gu, H. G.; Wang, J. X.; Zou, Y. J.; Qi, G. D.; Xu, J.; Deng, F.; Shen, W. J.; Li, J. et al. Beyond the thermal equilibrium limit of ammonia synthesis with dual temperature zone catalyst powered by solar light. *Chem* **2019**, *5*, 2702–2717.

[65] Guo, K.; Liu, D.; Zhang, Y.; Feng, H.; Li, Q. A full-spectrum-responsive metal-organic-framework-derived carbon-supported bimetallic catalyst for photothermal catalytic methane dry reforming. *Chem. Eng. J.* **2025**, *519*, 165155.

[66] Sun, N.; Liu, X. L.; Tian, C.; Xu, Q.; Xuan, Y. M. Selective plasmonic C–H bond editing for low-temperature light-driven greenhouse gas upgrading. *Adv. Energy Mater.* **2025**, *15*, 2404005.

[67] Ravi, M.; Ranocchiari, M.; van Bokhoven, J. A. The direct catalytic oxidation of methane to methanol-a critical assessment. *Angew. Chem., Int. Ed.* **2017**, *56*, 16464–16483.

[68] Ma, X. C.; Shi, Y. L.; Liu, J. Y.; Li, X. T.; Cui, X. F.; Tan, S. J.; Zhao, J.; Wang, B. Hydrogen-bond network promotes water splitting on the TiO_2 surface. *J. Am. Chem. Soc.* **2022**, *144*, 13565–13573.

[69] Liu, C. J.; Ye, J. Y.; Jiang, J. J.; Pan, Y. X. Progresses in the preparation of coke resistant Ni-based catalyst for steam and CO_2 reforming of methane. *ChemCatChem* **2011**, *3*, 529–541.

[70] Jiang, Y. H.; Li, S. Y.; Fan, X. Y.; Tang, Z. Y. Recent advances on aerobic photocatalytic methane conversion under mild conditions. *Nano Res.* **2023**, *16*, 12558–12571.

[71] Xie, J. J.; Jin, R. X.; Li, A.; Bi, Y. P.; Ruan, Q. S.; Deng, Y. C.; Zhang, Y. J.; Yao, S. Y.; Sankar, G.; Ma, D. et al. Highly selective oxidation of methane to methanol at ambient conditions by titanium dioxide-supported iron species. *Nat. Catal.* **2018**, *1*, 889–896.

[72] Luo, L.; Gong, Z. Y.; Xu, Y. X.; Ma, J. N.; Liu, H. F.; Xing, J. L.; Tang, J. W. Binary Au–Cu reaction sites decorated ZnO for selective methane oxidation to C1 oxygenates with nearly 100% selectivity at room temperature. *J. Am. Chem. Soc.* **2022**, *144*, 740–750.

[73] Luo, L. H.; Luo, J.; Li, H. L.; Ren, F. N.; Zhang, Y. F.; Liu, A. D.; Li, W. X.; Zeng, J. Water enables mild oxidation of methane to methanol on gold single-atom catalysts. *Nat. Commun.* **2021**, *12*, 1218.

[74] Chen, Y. Q.; Zhang, R. X.; Ren, M.; Jin, Y. X.; Wang, W. J.; Feng, J. Y.; Gao, Z. H.; Yan, Z. F.; Liu, Y. M.; Huang, W. et al. Photo-assisted thermal catalysis for methanol synthesis from methane oxidation on Cu-MOR/g-C_3N_4. *Fuel* **2023**, *340*, 127525.

[75] Wang, W. J.; Hao, J. C.; Liu, L.; Zhang, Z. X.; Huang, W.; Zuo, Z. J. Photothermal catalytic methane oxidation to methanol on Cu/Ti-ZSM-5. *Fuel* **2024**, *376*, 132720.

[76] Cao, Y. H.; Huang, Z. A.; Han, C. Q.; Zhou, Y. Product peroxidation inhibition in methane photooxidation into methanol. *Adv. Sci.* **2024**, *11*, 2306891.

[77] Fan, Y. Y.; Zhou, W. C.; Qiu, X. Y.; Li, H. D.; Jiang, Y. H.; Sun, Z. H.; Han, D. X.; Niu, L.; Tang, Z. Y. Selective photocatalytic oxidation of methane by quantum-sized bismuth vanadate. *Nat. Sustain.* **2021**, *4*, 509–515.

[78] Wang, M. J.; Jia, J.; Meng, Z. D.; Xia, J.; Hu, X. Y.; Xue, F.; Peng, H. P.; Meng, X. M.; Yi, J.; Chen, X. L. et al. Plasmonic Pd–Sb nanosheets for photothermal CH_4 conversion to HCHO and therapy. *Sci. Adv.* **2024**, *10*, eado9664.

[79] Wang, Y. X.; Zhang, Y. Y.; Wang, X. Q.; Liu, Y.; Wu, Z. B. Photothermal direct methane conversion to formaldehyde at the gas-solid interface under ambient pressure. *Nat. Commun.* **2025**, *16*, 2550.

[80] Zhang, R. X.; Shi, J. L.; Fu, L.; Liu, Y. G.; Jia, Y. B.; Han, Z. Y.; Yuan, K.; Jiang, H. Y. Direct photocatalytic methane oxidation to formaldehyde by N doping co-decorated mixed crystal TiO_2. *ACS Nano* **2024**, *18*, 12994–13005.

[81] Luo, L.; Han, X. Y.; Wang, K. R.; Xu, Y. X.; Xiong, L. Q.; Ma, J. N.; Guo, Z. X.; Tang, J. W. Nearly 100% selective and visible-light-driven methane conversion to formaldehyde via. single-atom Cu and $W^{\delta+}$. *Nat. Commun.* **2023**, *14*, 2690.

[82] Jiang, Y. H.; Zhao, W. S.; Li, S. Y.; Wang, S. K.; Fan, Y. Y.; Wang, F.; Qiu, X. Y.; Zhu, Y. F.; Zhang, Y.; Long, C. et al. Elevating photooxidation of methane to formaldehyde via TiO_2 crystal phase engineering. *J. Am. Chem. Soc.* **2022**, *144*, 15977–15987.

[83] Fan, Y. Y.; Jiang, Y. H.; Lin, H. T.; Li, J. N.; Xie, Y. J.; Chen, A. Y.; Li, S. Y.; Han, D. X.; Niu, L.; Tang, Z. Y. Insight into selectivity of photocatalytic methane oxidation to formaldehyde on tungsten trioxide. *Nat. Commun.* **2024**, *15*, 4679.

[84] Zhai, G. Y.; Yang, S. Y.; Chen, Y. H.; Xu, J. C.; Si, S. H.; Zhang, H. G.; Liu, Y. Y.; Ma, J.; Sun, X.; Huang, W. X. et al. Direct photocatalytic oxidation of methane to formic acid with high selectivity via a concerted proton-electron transfer process. *J. Am. Chem. Soc.* **2025**, *147*, 2444–2454.

[85] Sun, Z. W.; Wang, C. L.; Hu, Y. H. Highly selective photocatalytic conversion of methane to liquid oxygenates over silicomolybdic-acid/TiO_2 under mild conditions. *J. Mater. Chem. A* **2021**, *9*, 1713–1719.

[86] Dai, J.; Yang, J.; Leng, C. C.; Wang, Y.; Jia, H. L.; Zhang, G. Boosted selective photooxidation of methane to methanol on Bi_2S_3/BiOCl–O_V heterojunctions with atomic co-sharing interface via synergy of S-scheme charge transfer and photothermal effect. *J. Colloid Interface Sci.* **2025**, *699*, 138228.

[87] Zhou, P.; Navid, I. A.; Xiao, Y. X.; Ye, Z. W.; Dong, W. J.; Wang, P.; Sun, K.; Mi, Z. T. Metal-support interaction-promoted photothermal catalytic methane reforming into liquid fuels. *J. Phys. Chem. Lett.* **2022**, *13*, 8122–8129.

[88] Song, S.; Song, H.; Li, L. M.; Wang, S. Y.; Chu, W.; Peng, K.; Meng, X. G.; Wang, Q.; Deng, B. W.; Liu, Q. X. et al. A selective Au–ZnO/TiO_2 hybrid photocatalyst for oxidative coupling of methane to ethane with dioxygen. *Nat. Catal.* **2021**, *4*, 1032–1042.

[89] Wang, Y. L.; Hu, P.; Yang, J.; Zhu, Y. A.; Chen, D. C–H bond activation in light alkanes: A theoretical perspective. *Chem. Soc. Rev.* **2021**, *50*, 4299–4358.

[90] Shen, T. Y.; Hu, S. Y.; Sun, X. L.; Liu, G. H.; Song, Z. H.; Wu, Z. H.; Zheng, L. R.; Song, Y. F. Unraveling the synergy of Au and polar MgO(111) surface in photothermal catalytic oxidative coupling of methane. *Adv. Funct. Mater.* **2025**, *35*, 2418021.

[91] Singh, S. P.; Anzai, A.; Kawaharasaki, S.; Yamamoto, A.; Yoshida, H. Non-oxidative coupling of methane over Pd-loaded gallium oxide photocatalysts in a flow reactor. *Catal. Today* **2021**, *375*, 264–272.

[92] Kumar, A. A review on the factors affecting the photocatalytic degradation of hazardous materials. *Mater. Sci. Eng. Int. J.* **2017**, *1*, 106–114.

[93] Meng, F. P.; Liu, Y. Z.; Wang, J.; Tan, X. Y.; Sun, H. Q.; Liu, S. M.; Wang, S. B. Temperature dependent photocatalysis of g-C_3N_4, TiO_2 and ZnO: Differences in photoactive mechanism. *J. Colloid Interface Sci.* **2018**, *532*, 321–330.

[94] Zhang, P.; Li, J. W.; Huang, H. W.; Sui, X.; Zeng, H. H.; Lu, H. J.; Wang, Y.; Jia, Y. Y.; Steele, J. A.; Ao, Y. H. et al. Platinum single-atom nests boost solar-driven photocatalytic non-oxidative coupling of methane to ethane. *J. Am. Chem. Soc.* **2024**, *146*, 24150–24157.

[95] Chen, Z. Y.; Wu, S. Q.; Ma, J. Y.; Mine, S.; Toyao, T.; Matsuoka, M.; Wang, L. Z.; Zhang, J. L. Non-oxidative coupling of methane: N-type doping of niobium single atoms in TiO_2–SiO_2 induces electron localization. *Angew. Chem., Int. Ed.* **2021**, *60*, 11901–11909.

[96] Ma, J. Y.; Zhang, Q. Q.; Chen, Z. Y.; Kang, K.; Pan, L. H.; Wu, S. Q.; Chen, C.; Wu, Z. Q.; Zhang, J. L.; Wang, L. Z. Design of frustrated Lewis pair in defective TiO_2 for photocatalytic non-oxidative methane coupling. *Chem Catal.* **2022**, *2*, 1775–1792.

[97] Chen, Z. Y.; Ye, Y. T.; Feng, X. Y.; Wang, Y.; Han, X. W.; Zhu, Y.; Wu, S. Q.; Wang, S. Y.; Yang, W. D.; Wang, L. Z. et al. High-density frustrated Lewis pairs based on Lamellar Nb_2O_5 for photocatalytic non-oxidative methane coupling. *Nat. Commun.* **2023**, *14*, 2000.

[98] Yan, Z. Y.; Li, X. N.; Guan, X. W.; Wang, Z. L.; Shen, J. N.; Yan, T. J.; Ma, T. Y.; Zhang, Z. Z. Boosting photothermal catalytic non-oxidative methane coupling by high-density frustrated Lewis pairs in Ag/InO_xH_y. *J. Catal.* **2025**, *447*, 116117.

[99] Xue, F.; Zhang, C. Y.; Cheng, C.; Yan, X. L.; Liu, F.; Liu, X. Z.; Jiang, B.; Zhang, Q. Y.; Sun, L.; Peng, H. P. et al. Selective light-driven methane oxidation to ethanol. *Nat. Commun.* **2024**, *15*, 10451.

[100] Li, Y. N.; Liu, H.; Mao, J.; Gao, M.; Zhang, Y. L.; Zhao, Q.; Liu, M.; Song, Y.; Hu, J. T.; Zhang, W. W. et al. MoS_2-confined Rh–Zn atomic pair boosts photo-driven methane carbonylation to acetic acid. *Nat. Commun.* **2025**, *16*, 487.

[101] Zhou, Y. Y.; Zhang, L.; Wang, W. Z. Direct functionalization of methane into ethanol over copper modified polymeric carbon nitride via photocatalysis. *Nat. Commun.* **2019**, *10*, 506.

[102] Du, J.; Chen, W.; Wu, G. F.; Song, Y. F.; Dong, X.; Li, G. H.; Fang, J. H.; Wei, W.; Sun, Y. H. Evoked methane photocatalytic conversion to C2 oxygenates over ceria with oxygen vacancy. *Catalysts* **2020**, *10*, 196.

[103] Du, X. Y.; Yang, Z. S.; Yang, X. M.; Zhang, Q. Q.; Liu, L. Q.; Ye, J. H. Efficient photocatalytic conversion of methane into ethanol over P-doped g-C_3N_4 under ambient conditions. *Energy Fuels* **2022**, *36*, 3929–3937.

[104] Yang, Z. S.; Zhang, Q. Q.; Ren, L. T.; Chen, X.; Wang, D. F.; Liu, L. Q.; Ye, J. H. Efficient photocatalytic conversion of CH_4 into ethanol with O_2 over nitrogen vacancy-rich carbon nitride at room temperature. *Chem. Commun.* **2021**, *57*, 871–874.

[105] Li, N. X.; Li, Y.; Jiang, R. M.; Zhou, J. C.; Liu, M. C. Photocatalytic coupling of methane and CO_2 into C2-hydrocarbons over Zn doped g-C_3N_4 catalysts. *Appl. Surf. Sci.* **2019**, *498*, 143861.

[106] Feng, G. H.; Zhao, Y. H.; Ma, C. J.; Chen, W.; Li, T.; Zhao, X. J.; Li, G. H.; Dong, X.; Song, Y. F.; Wei, W. et al. Solar driven efficient direct conversion of methane to multicarbon oxygenates. *J. Mater. Chem. A* **2022**, *10*, 7856–7868.

[107] Wang, J. X.; Zhang, L.; Zeng, D.; Wang, W. J.; Li, R. F.; Jia, T. K.; Cui, B. K.; Chu, H. X.; Wang, W. Z. Multi-radicals mediated one-step conversion of methane to acetic acid via photocatalysis. *Appl. Cata. B: Environ.* **2023**, *337*, 122983.

[108] Shan, J. J.; Li, M. W.; Allard, L. F.; Lee, S.; Flytzani-Stephanopoulos, M. Mild oxidation of methane to methanol or acetic acid on supported isolated rhodium catalysts. *Nature* **2017**, *551*, 605–608.

[109] Xue, Y.; Wang, Y. J.; Yang, Z. J.; Li, T.; Jin, H. F.; Peng, Y. K.; Peng, Y.; Zhao, Y. F. Solar-driven methane coupling to ethane over

layered double hydroxide-based heterojunction photothermal catalysts. *Ind. Eng. Chem. Res.* **2025**, *64*, 4784–4793.

[110] Bai, Z. J.; Yan, R. L.; Gao, X. H.; Xie, G. M.; Song, H.; Ye, J. H.; Wang, Z. J. Au-decorated Nb_2O_5 featuring unsaturated niobium centers and photoinduced oxygen vacancies for photocatalytic oxidative coupling of methane to C_{2+} hydrocarbons. *Angew. Chem., Int. Ed.* **2025**, *64*, e202512269.

[111] Shen, T. Y.; Wang, Z. L.; Xu, S. M.; Sun, X. L.; Liu, G. H.; Bai, S.; Li, J. X.; Song, Z. H.; Zheng, L. R.; Song, Y. F. A noble-metal-free, nickel(II)-doped MgO/Al_2O_3 catalyst for highly selective photothermal coupling of methane to ethane. *Cell Rep. Phys. Sci.* **2023**, *4*, 101478.

[112] Song, Y.; Ozdemir, E.; Ramesh, S.; Adishev, A.; Subramanian, S.; Harale, A.; Albuali, M.; Fadhel, B. A.; Jamal, A.; Moon, D. et al. Dry reforming of methane by stable Ni–Mo nanocatalysts on single-crystalline MgO. *Science* **2020**, *367*, 777–781.

[113] Chen, S.; Pei, C. L.; Gong, J. L. Insights into interface engineering in steam reforming reactions for hydrogen production. *Energy Environ. Sci.* **2019**, *12*, 3473–3495.

[114] Yang, R. J.; He, C. X.; Dong, Y.; Chen, W. H.; Chen, L. Y.; Wang, Z. H.; Kan, M.; Wu, S. Q.; Zhang, J. L. Photothermal methane dry reforming: Catalyst architectures, mechanistic pathways, and future challenges. *Chem. Soc. Rev.* **2025**, *54*, 11017–11060.

[115] Bian, J.; Zhang, Z. Q.; Liu, Y.; Chen, E. Q.; Tang, J. W.; Jing, L. Q. Strategies and reaction systems for solar-driven CO_2 reduction by water. *Carbon Neutrality* **2022**, *1*, 5.

[116] Song, H.; Meng, X. G.; Dao, T. D.; Zhou, W.; Liu, H. M.; Shi, L.; Zhang, H. B.; Nagao, T.; Kako, T.; Ye, J. H. Light-enhanced carbon dioxide activation and conversion by effective plasmonic coupling effect of Pt and Au nanoparticles. *ACS Appl. Mater. Interfaces* **2018**, *10*, 408–416.

[117] Liu, H. M.; Meng, X. G.; Dao, T. D.; Zhang, H. B.; Li, P.; Chang, K.; Wang, T.; Li, M.; Nagao, T.; Ye, J. H. Conversion of carbon dioxide by methane reforming under visible-light irradiation: Surface-plasmon-mediated nonpolar molecule activation. *Angew. Chem., Int. Ed.* **2015**, *54*, 11545–11549.

[118] Du, K.; Guo, J. Q.; Song, C. X.; Liu, X.; Chen, M. J.; Yuan, D. C.; Ye, R. P.; San, X. Y.; Li, Y. G.; Ye, J. H. Persistent photothermal CO_2 methanation without external energy input. *Energy Environ. Sci.* **2025**, *18*, 1255–1261.

[119] Han, B.; Wei, W.; Chang, L.; Cheng, P. F.; Hu, Y. H. Efficient visible light photocatalytic CO_2 reforming of CH_4. *ACS Catal.* **2016**, *6*, 494–497.

[120] Liu, H. M.; Song, H.; Zhou, W.; Meng, X. G.; Ye, J. H. A promising application of optical hexagonal TaN in photocatalytic reactions. *Angew. Chem., Int. Ed.* **2018**, *57*, 16781–16784.

[121] Liu, H. M.; Meng, X. G.; Dao, T. D.; Liu, L. Q.; Li, P.; Zhao, G. X.; Nagao, T.; Yang, L. Q.; Ye, J. H. Light assisted CO_2 reduction with methane over SiO_2 encapsulated Ni nanocatalysts for boosted activity and stability. *J. Mater. Chem. A* **2017**, *5*, 10567–10573.

[122] Pan, F. P.; Xiang, X. M.; Du, Z. C.; Sarnello, E.; Li, T.; Li, Y. Integrating photocatalysis and thermocatalysis to enable efficient CO_2 reforming of methane on Pt supported CeO_2 with Zn doping and atomic layer deposited MgO overcoating. *Appl. Catal. B: Environ.* **2020**, *260*, 118189.

[123] Pan, F. P.; Xiang, X. M.; Deng, W.; Zhao, H. L.; Feng, X. H.; Li, Y. A novel photo-thermochemical approach for enhanced carbon dioxide reforming of methane. *ChemCatChem* **2018**, *10*, 940–945.

[124] Rao, Z. Q.; Cao, Y. H.; Huang, Z. A.; Yin, Z. H.; Wan, W. C.; Ma, M. Z.; Wu, Y. X.; Wang, J. B.; Yang, G. D.; Cui, Y. et al. Insights into the nonthermal effects of light in dry reforming of methane to enhance the H_2/CO ratio near unity over Ni/Ga_2O_3. *ACS Catal.* **2021**, *11*, 4730–4738.

[125] Cao, H. M.; Li, Y. Z.; Hu, Q. Q.; Wu, J. C.; Ji, L. A novel strategy for dramatically improving catalytic performance for light-driven thermocatalytic CO_2 reduction with CH_4 on Ru/MgO: The CO_2 molecular fencing effect promoted by photoactivation. *J. Mater. Chem. A* **2023**, *11*, 19645–19655.

[126] Yin, Q.; Shen, T. Y.; Li, J. H.; Ning, C. J.; Xue, Y.; Chen, G. B.; Xu, M.; Wang, F. L.; Song, Y. F.; Zhao, Y. F. et al. Solar-driven dry reforming of methane using RuNi single-atom alloy catalyst coupled with thermal decomposition of carbonates. *Chem. Eng. J.* **2023**, *470*, 144416.

[127] Yao, Y.; Li, B.; Gao, X. W.; Yang, Y. Y.; Yu, J. B.; Lei, J. N.; Li, Q.; Meng, X. C.; Chen, L. X.; Xu, D. S. Highly efficient solar-driven dry reforming of methane on a $Rh/LaNiO_3$ catalyst through a light-induced metal-to-metal charge transfer process. *Adv. Mater.* **2023**, *35*, 2303654.

[128] Nie, W. F.; Chen, L. W.; Hao, Y. C.; Ge, X. J.; Liu, H. D.; Li, J. N.; Wang, J. L.; Wang, Z.; Huang, H. Z.; Sun, C. et al. Photocatalytic oxidative coupling of methane to C_3+ hydrocarbons via nanopore-confined microenvironments. *Nat. Energy* **2025**, *10*, 1095–1106.

[129] Fei, M. C.; Chen, B. Q.; Sakamoto, Y.; Wang, L. Z.; Mu, Y.; Zhang, J. W.; Wilkes, J. R.; Gallenstein, R.; Huang, J.; Bao, J. L. et al. Direct formation of C_3 oxygenates through photocatalytic CH_4–CO coupling. *J. Am. Chem. Soc.* **2025**, *147*, 25834–25840.

[130] Wang, C.; Xu, Y. X.; Tang, J. W. Catalytic methane removal to mitigate its environmental effect. *Sci. China Chem.* **2023**, *66*, 1032–1051.

[131] Geng, Z. J.; Yu, Y. F.; Offen, A. J.; Liu, J. Achieving maximum overall light enhancement in plasmonic catalysis by combining thermal and non-thermal effects. *Nat. Catal.* **2023**, *6*, 1241–1247.

[132] Li, X. Q.; Zhang, X.; Everitt, H. O.; Liu, J. Light-induced thermal gradients in ruthenium catalysts significantly enhance ammonia production. *Nano Lett.* **2019**, *19*, 1706–1711.

[133] Mascaretti, L.; Schirato, A.; Montini, T.; Alabastri, A.; Naldoni, A.; Fornasiero, P. Challenges in temperature measurements in gas-phase photothermal catalysis. *Joule* **2022**, *6*, 1727–1732.

[134] Filez, M.; De Coster, V.; Poelman, H.; Briois, V.; Beauvois, A.; Dendooven, J.; Roeffaers, M. B. J.; Galvita, V.; Detavernier, C. Selectively monitoring the operando temperature of active metal nanoparticles during catalytic reactions by X-ray absorption nanothermometry. *Nat. Catal.* **2025**, *8*, 187–195.

[135] Jacobs, T. S.; van Swieten, T. P.; Vonk, S. J. W.; Bosman, I. P.; Melcherts, A. E. M.; Janssen, B. C.; Janssens, J. C. L.; Monai, M.; Meijerink, A.; Rabouw, F. T. et al. Mapping temperature heterogeneities during catalytic CO_2 methanation with *Operando* luminescence thermometry. *ACS Nano* **2023**, *17*, 20053–20061.

[136] Jiang, W. B.; Low, J.; Mao, K. K.; Duan, D. L.; Chen, S. M.; Liu, W.; Pao, C. W.; Ma, J.; Sang, S. K.; Shu, C. et al. Pd-modified ZnO–Au enabling alkoxy intermediates formation and dehydrogenation for photocatalytic conversion of methane to ethylene. *J. Am. Chem. Soc.* **2021**, *143*, 269–278.

[137] Si, J. Q.; Zhao, G. F.; Sun, W. D.; Liu, J. C.; Guan, C. R.; Yang, Y.; Shi, X. R.; Lu, Y. Oxidative coupling of methane: Examining the inactivity of the MnO_x–Na_2WO_4/SiO_2 catalyst at low temperature. *Angew. Chem., Int. Ed.* **2022**, *61*, e202117201.

[138] Li, L.; Fan, S. Z.; Mu, X. Y.; Mi, Z. T.; Li, C. J. Photoinduced conversion of methane into benzene over GaN nanowires. *J. Am. Chem. Soc.* **2014**, *136*, 7793–7796.

[139] Jin, P.; Guo, P.; Luo, N. C.; Zhang, H.; Ni, C. W.; Chen, R. T.; Liu, W.; Li, R. G.; Xiao, J. P.; Wang, G. X. et al. Photochemical H_2 dissociation for nearly quantitative CO_2 reduction to ethylene. *Science* **2025**, *389*, 1037–1042.

[140] Peh, C. K. N.; Gao, M. M.; Ho, G. W. Harvesting broadband absorption of the solar spectrum for enhanced photocatalytic H_2 generation. *J. Mater. Chem. A* **2015**, *3*, 19360–19367.

[141] Westrich, T. A.; Dahlberg, K. A.; Kaviany, M.; Schwank, J. W. High-temperature photocatalytic ethylene oxidation over TiO_2. *J. Phys. Chem. C* **2011**, *115*, 16537–16543.

[142] Yang, J. R.; Wang, D. S. Multi-atomic catalysts: Pioneering applications in the pursuit of carbon neutrality. *Carbon Future* **2024**, *1*, 9200019.

[143] Sun, W.; Cao, X. E. Photothermal CO_2 catalysis: From catalyst discovery to reactor design. *Chem Catal.* **2022**, *2*, 215–217.

[144] Chen, C.; Jiao, F.; Lu, B. C.; Liu, T. X.; Liu, Q. B.; Jin, H. G. Challenges and perspectives for solar fuel production from water/carbon dioxide with thermochemical cycles. *Carbon Neutrality* **2023**, *2*, 9.

[145] Nishiyama, H.; Yamada, T.; Nakabayashi, M.; Maehara, Y.; Yamaguchi, M.; Kuromiya, Y.; Nagatsuma, Y.; Tokudome, H.; Akiyama, S.; Watanabe, T. et al. Photocatalytic solar hydrogen production from water on a 100-m^2 scale. *Nature* **2021**, *598*, 304–307.

[146] Zoller, S.; Koepf, E.; Nizamian, D.; Stephan, M.; Patané, A.; Haueter, P.; Romero, M.; González-Aguilar, J.; Lieftink, D.; de Wit, E. et al. A solar tower fuel plant for the thermochemical production of kerosene from H_2O and CO_2. *Joule* **2022**, *6*, 1606–1616.

[147] Mai, H.; Le, T. C.; Chen, D. H.; Winkler, D. A.; Caruso, R. A. Machine learning for electrocatalyst and photocatalyst design and discovery. *Chem. Rev.* **2022**, *122*, 13478–13515.

Data availability

Not applicable.

Acknowledgments

Y. L and X. L. are thankful for the funding from the European Union's Horizon Europe research and innovation programme under grant agreement No 101070721 (project acronym "GH2")

Author contributions

Y. L. and X. L. supervised the study. C. G. and X. L. co-wrote the manuscript. Y. L. revised the manuscript. All authors have approved the final version of the manuscript.

Competing Interests

The authors have no competing interests to declare that are relevant to the content of this article.

Use of AI statement

None.

Open Access This article is licensed under the terms of the Creative Commons Attribution 4.0 International License (http://creativecommons.org/licenses/by/4.0/), which permits use, sharing, distribution and reproduction in any medium, provided the original work is properly cited.

© The author(s) 2026. Published by Tsinghua University Press.